Neutron tagging following atmospheric neutrino events in a water Cherenkov detector

Published by IOP Publishing for Sissa Medialab

Received: *July 17, 2022*
Revised: *September 18, 2022*
Accepted: *September 18, 2022*
Published: *October 18, 2022*

2022 JINST 17 P10029

Neutron tagging following atmospheric neutrino events in a water Cherenkov detector

The Super-Kamiokande Collaboration

E-mail: hayato@icrr.u-tokyo.ac.jp

Abstract: We present the development of neutron-tagging techniques in Super-Kamiokande IV using a neural network analysis. The detection efficiency of neutron capture on hydrogen is estimated to be 26%, with a mis-tag rate of 0.016 per neutrino event. The uncertainty of the tagging efficiency is estimated to be 9.0%. Measurement of the tagging efficiency with data from an Americium-Beryllium calibration agrees with this value within 10%. The tagging procedure was performed on 3,244.4 days of SK-IV atmospheric neutrino data, identifying 18,091 neutrons in 26,473 neutrino events. The fitted neutron capture lifetime was measured as $218 \pm 9\,\mu$s.

Keywords: Particle identification methods; Cherenkov detectors; Neutrino detectors; Large detector systems for particle and astroparticle physics

https://doi.org/10.1088/1748-0221/17/10/P10029

Contents

2022 JINST 17 P10029

1 Introduction

The Super-Kamiokande (SK) water Cherenkov detector is utilized to study a wide range of physics; it has measured neutrinos from various sources (solar [1], atmospheric [2], and accelerator [3]), while searching for nucleon decay [4] and supernova neutrinos [5]. While SK efficiently detects relativistic charged particles with small masses, like electrons, muons, and pions, heavy particles with low momentum or no charge, such as protons and neutrons, produce little or no Cherenkov light and cannot be easily detected. However, the ability to detect neutrons, though challenging, is expected to improve the sensitivity of various analyses [6]. As an example, the detection of neutrons can improve the statistical separation of neutrinos and anti-neutrinos since neutrino events are expected to produce fewer neutrons than anti-neutrino events. The clearest example is the anti-neutrino charged current quasi-elastic (CCQE) interaction, which produces neutron in the final state but the neutrino CCQE produces proton instead. Improving this separation can enhance sensitivity to the neutrino mass ordering via analysis of atmospheric neutrino oscillations. Further, the observed number of neutrons is correlated with the incident neutrino energy, making it possible to improve estimations of the parent energy in atmospheric neutrino interactions. Detection of neutrons can also help to reduce backgrounds to nucleon decay searches, since their main backgrounds, atmospheric neutrino events, are frequently associated with neutrons, while neutron ejection from nucleon decay in oxygen is expected to be rare. Neutron tagging has been demonstrated as a powerful tool for background reduction in recent nucleon decay searches [7].

The neutron detection method presented here relies on observing the gamma ray produced in neutron capture on hydrogen. Neutrino or anti-neutrino interaction produces neutrons and the produced neutrons travel in the SK water and thermalized. The thermalized neutron will eventually be captured by an oxygen or hydrogen nucleus, with capture cross sections of 0.19 mb and 0.33 b, respectively. Therefore, almost all the neutrons are captured by hydrogen, with a characteristic capture time of $204.8 \pm 0.4\,\mu$s [8]. This results in the emission of a 2.2 MeV gamma ray,

$$n + p \rightarrow d + \gamma\,(2.2\,\mathrm{MeV}) \tag{1.1}$$

as shown in figure 1.

The gamma ray may then scatter electrons (Compton scattering) in the water, accelerating some of them above the Cherenkov threshold. Identifying the light from those electrons can be used to infer the presence of the gamma ray and hence its parent neutron. However, it is not simple to identify

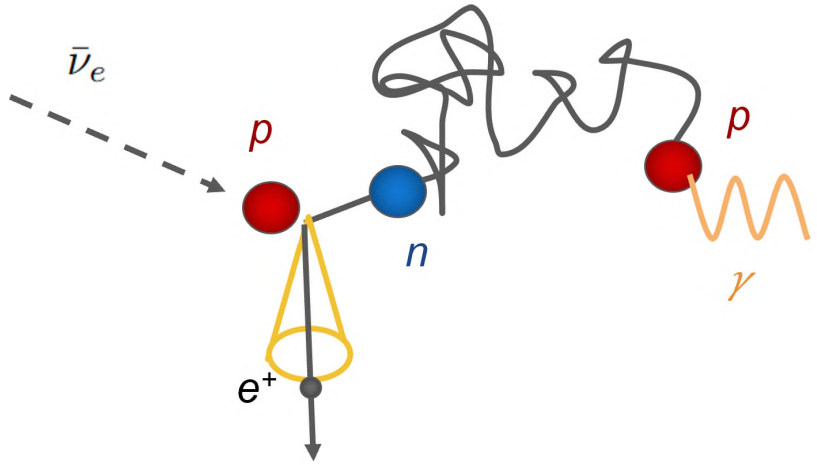

Figure 1. A sketch of neutron production and capture by hydrogen. Anti-neutrino charged current quasi-elastic scattering produces a neutron. The neutron travels in the SK detector (water), thermalized, and eventually capture by hydrogen. When the neutron is captured by hydrogen, 2.2 MeV gamma ray is emitted.

2.2 MeV gamma rays from neutron captures on hydrogen; the conventional event reconstruction threshold at SK is ~ 4 MeV, which corresponds to 34 hit PMTs, while the typical number of hits from a 2.2 MeV gamma ray is 7. As a result of our inability to fully reconstruct neutron captures on hydrogen, we instead developed dedicated neutron tagging techniques. This neutron tagging technique was first demonstrated in SK in 2009 [9] as a means to reduce background events in the search for supernova relic neutrinos [5]. Neutron tagging was used in previous atmospheric neutrino and proton decay analyses by Super-Kamiokande [10–12]. However, a detailed description of the neural network has not yet been published. In this paper we provide that description. We also document improvements and extensions being used for current analyses. Differences between the present method and that used in previous analysis's are described in section D. In this paper we also demonstrate the performance of the algorithm by applying our tagging algorithm to atmospheric neutrino MC and data.

2 Super-Kamiokande

2.1 Detector

Super-Kamiokande is located 1,000 meters (2,700 meters-water-equivalent) below Mount Ikenoyama in Gifu, Japan [13]. It consists of a 50 kiloton (kton) cylindrical tank filled with ultra-pure water, which is divided into a 32 kton inner detector (ID) surrounded by an 18 kton outer detector (OD). The ID and the OD are optically separated by Tyvek sheeting. The ID is observed by 11,129 inward-facing 20-inch photo multiplier tubes (PMTs), while the OD is observed by 1,885 outward-facing 8-inch PMTs. The ID provides most of the information used in event reconstruction, while the OD is used as an active cosmic ray veto and to provide information regarding particles escaping from the ID.

2.2 Event categories

Generally speaking, events in SK with more than 100 MeV of deposited energy in the detector are separated into three categories during data reduction. Fully-contained (FC) events are events with

2022 JINST 17 P10029

PMT activity only in the ID. Partially-contained (PC) events have activity in both the ID and the OD but are reconstructed to have originated from inside the ID. Upward-going muon (UPMU) events are events with both ID and OD activity but which are reconstructed to have originated from outside the ID and enter from below the horizon. Accordingly, nearly all UPMU events are muons from neutrino interactions in the rock around the detector. In this paper, the neutron tagging method is only applied to the FC event sample.

2.3 Triggers and events

The SK data acquisition system was upgraded for the start of the SK-IV run period from October 6th, 2008 [14]. The hardware trigger used during the previous periods, SK I-III, was replaced with a software trigger in SK-IV. This new software trigger allows different timing gate widths to be set depending on the nature of a particular event. There are five standard triggers used in SK-IV, which are summarized in table 1. For example, the SHE (Super High Energy) trigger threshold of 70 hits (reduced to 58 hits later on in SK-IV) in a 200 ns window corresponds to the number of hits an electron of about 10 MeV (8 MeV) produces in the detector. While the 40 µs gate width of the SHE trigger is long enough to record the hits from relativistic particles and their decay products, the longer neutron capture lifetime means that only around 15% of thermal neutrons are captured before the end of the SHE gate. In order to detect hits from later neutron captures, all SHE triggers which do not have a corresponding OD trigger are followed by an additional trigger called AFT (AFTer trigger), which records from 35 µs to 535 µs after the SHE trigger was issued. At the beginning of SK-IV, the event gate width was up to 385 µs, instead of 535 µs. During this period, the efficiency is $\sim$ 14% lower than the later data taking period with the longer event gate width. However, this configuration was used for just 30 days, representing less than 1% of the current data set. Therefore, the effect of this period is neglected in the discussions that follow. In order to reduce the total amount of data, the AFT trigger is not issued following an OD trigger, because an OD trigger indicates that the event is not categorized as FC but as cosmic ray, PC, or UPMU. As a result, the neutron tagging method can only be applied to FC atmospheric neutrino or nucleon decay candidate events. We estimate that the combined SHE and AFT triggers cover 93% of neutron captures from FC events.

Table 1. Trigger information for SK-IV. The abbreviations are as follows: OD (Outer Detector), SLE (Super Low Energy), HE (High Energy), SHE (Super High Energy) and AFT (After). There are ~9 hits of dark noise in 200 ns, and 6 hits correspond to ~1 MeV electron-equivalent energy. There are two trigger threshold values for SLE and SHE in the table. In the beginning of SK4, we set the threshold of SLE to 34 hits but later the threshold value was lowered by 3 hits. Similarly, the SHE threshold was changed from 70 to 58 during SK4.

SK-IV Triggers	Hits/200 ns Threshold	Event Width (µs)
OD	22 (in OD)	$-5 \rightarrow 35$
SLE	34–31	$-0.5 \rightarrow 1.0$
HE	50	$-5 \rightarrow 35$
SHE	70–58	$-5 \rightarrow 35$
AFT	SHE, no OD	$35 \rightarrow 535$

3 Simulation

The atmospheric neutrino Monte-Carlo (MC), corresponding to a 500 years exposure of the detector, is used to optimize and estimate the performance of the neutron-tagging software. The atmospheric neutrino flux is provided by Honda et al. [15]. The interactions of neutrinos in water are simulated using the NEUT simulation software (v5.3.6) [2, 16]. NEUT also simulates nuclear interactions to propagate particles through the nuclei in which they were created. Particles are then propagated through the detector; its response is simulated by a GEANT3 [17] based simulation of SK called SKDETSIM [18]. Hadrons except for low momentum pions are simulated by the GEANT3 interface with the CALOR [19] package, which uses HETC [20] for hadrons below 10 GeV, FLUKA (GFLUKA) [21] for hadrons above 10 GeV, and MICAP [22] for neutrons below 20 MeV. The propagation of pions below 500 MeV/c in the water are simulated by NEUT. The low energy cutoff for neutral hadrons is set to 10^{-5} eV so that neutrons continue to be simulated until they are captured.

Uncorrelated PMT dark noise is the only source of background hits simulated by SKDETSIM. PMT after-pulsing, which occurs between 12 and 18 µs, creates a slight increase in the hit rate as seen in figure 2, but it is not modeled in SKDETSIM. Therefore, the search for neutron capture begins 18 µs after the primary trigger in order to avoid possible biases due to this after-pulsing. Based on the MC result, assuming the previously measured capture lifetime of neutrons in water, 204.8 µs [8], this reduces the maximum efficiency for neutron capture from 93% to 84%. Other low energy sources in the detector, such as radioactive decays from the surrounding rock, radon contamination in the water, and radioactive contaminants in the tank structure [23, 24] also generate random background hits. These backgrounds do not affect the reconstruction of higher energy particles, so they have been neglected in the simulation program for the atmospheric neutrino samples. In addition, hits from low energy sources are correlated in space and time, yet the low energy sources are difficult to model. Background hits from low energy backgrounds could mimic a 2.2 MeV gamma ray signal from neutron capture, which only produces around 7 hits in the detector. Therefore, it is necessary to accurately account for them. Our method is to overlay randomly triggered data events to account for both noise from the PMTs and these unmodeled processes.

In total, about 1.9 million random trigger events with a gate width of 1 ms were collected in 2009. When an MC event is produced, PMT dark noise is simulated by SKDETSIM up to 18 µs and thereafter the dark noise is provided by real hits from the random trigger events. The 900 ns channel dead-time of the SK-IV digitizer is modeled by removing any hit occurring less than 900 ns after a previous hit. This hybrid MC technique is illustrated in figure 3. Our 500 year MC samples contain about 2.5 million FC events, which means that some random trigger events are shared between two MC events due to the shortage of the random trigger events. In these cases the first 517 µs of a random trigger event is used for one event and the hits from 483 µs to 1 ms are used for the other event, a slight overlap with negligible effect on the analysis.

4 Neutron tagging algorithm

Before the neutron tagging is performed, all FC events are analyzed using the standard SK atmospheric neutrino event reconstruction software (APFit) [18]. This software reconstructs information associated with the primary event, including finding its vertex position in the detector,

2022 JINST 17 P10029

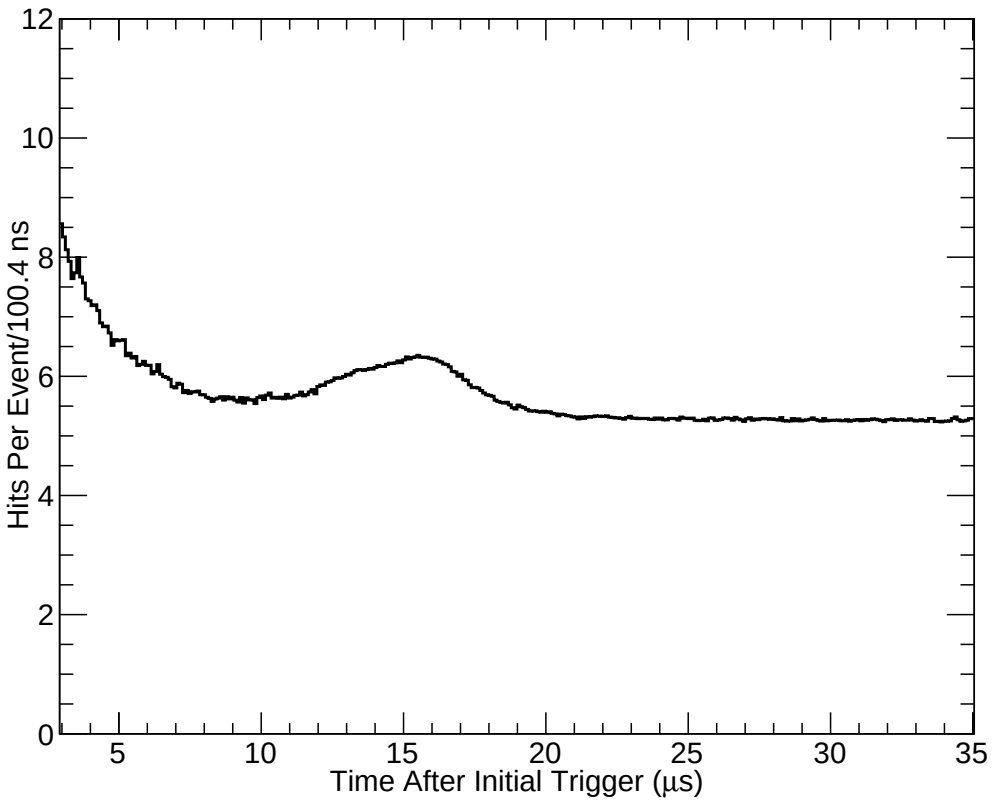

Figure 2. Hit rates over the course of an event, taken from the average of SK-IV events. Note the suppressed zero on the x-axis. The falling exponential on the left of the plot is due to decay electrons. The increase due to PMT after-pulsing in the 12 to 18 μs region can be clearly seen. After the PMT after-pulsing, the hit rate is flat for the rest of the event window.

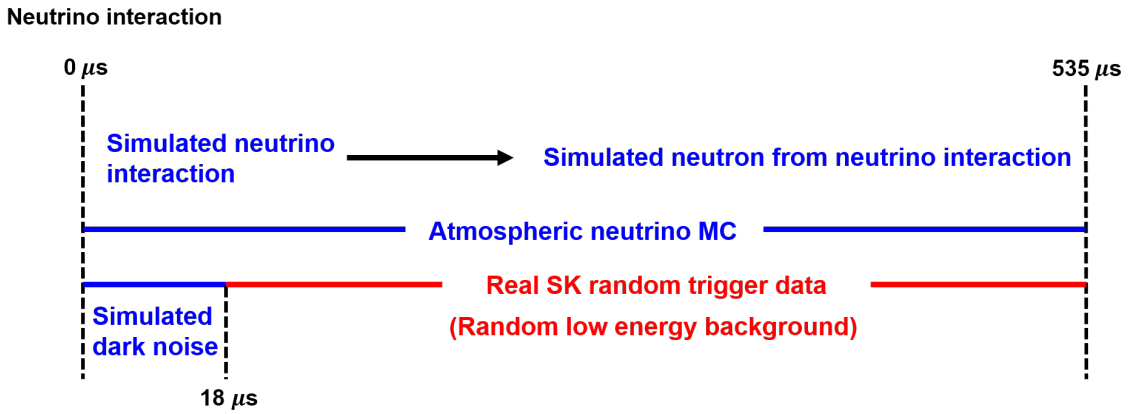

Figure 3. Diagram of MC construction procedure. Random trigger data are superimposed on simulated PMT hits from neutron capture events 18 μs after the primary interaction.

counting the number of the Cherenkov rings, identifying each Cherenkov ring as showering-like or non-showering-like, reconstructing its momentum, and finding π^0 candidates and decay electrons. Neutron tagging is then performed as a two-step process. Approximately seven Cherenkov photons are expected to be detected from a 2.2 MeV γ, as shown in figure 4. The number of hits in 10 ns after time-of-flight (ToF) subtraction is slightly smaller than the total number of PMT hits even though the duration of the Cherenkov photon emission is nearly instantaneous. This is because some of the Cherenkov photons are scattered in the detector and as a result travel a longer distance before detection. Therefore, the first step in the neutron tagging process is to search in time for clusters of

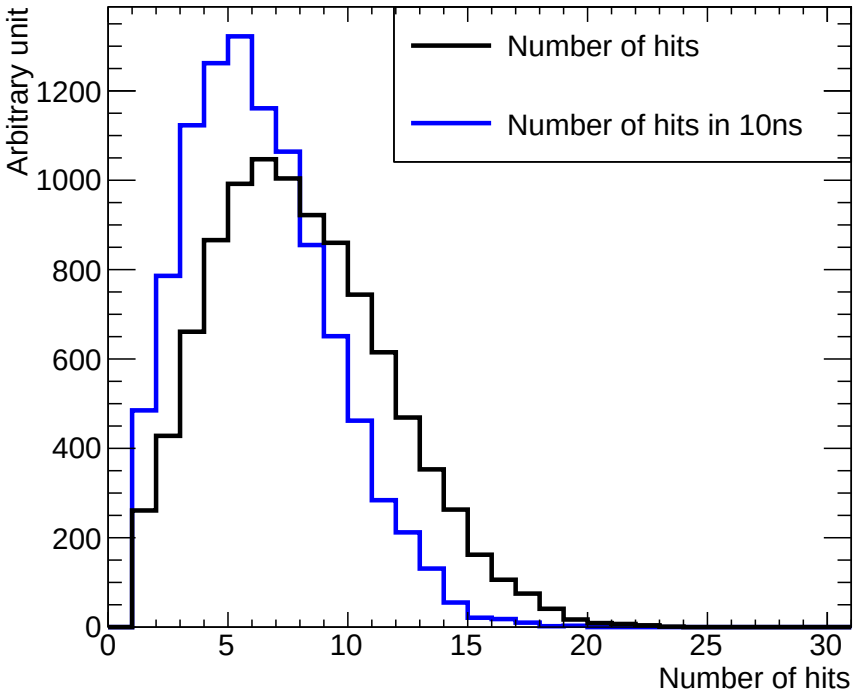

Figure 4. Number of hit PMTs in SK for 2.2 MeV γ using the SK detector simulation program. No noise is simulated and only the Cherenkov photons from the 2.2 MeV γ are recorded. The black histogram shows the total number of PMT hits. The blue histogram shows the largest number of hit PMTs in 10 ns obtained by using the 10 ns sliding window. In searching for the largest number of hit PMTs, the time-of-flight (ToF) from the generated point of 2.2 MeV γ is subtracted from each timing of PMT hit.

hit PMTs. These clusters are chosen as candidate neutron captures. During the second step, a neural network is used to differentiate real neutron capture candidates from backgrounds. Details of the neural network are described in section 4.2.

4.1 Step one: initial candidate selection

The MC sample shows that 70% of neutrons are captured within 200 cm of the initial interaction vertex. In the search for clusters of hits in time, each PMT's hit timing is corrected for each photon's ToF from the primary event vertex (neutrino vertex), which is reconstructed by APFit, to give a residual time.

A 10 ns sliding window is then used to search for clusters of hits in the residual time. This width was selected to take into account the distance from the actual neutron capture to the neutrino vertex, the 2.2 ns timing resolution of the PMT, and contamination from accidental background hits, which is expected to be ~ 0.5 hits per event in a 10 ns window. If there are five or more hits in the 10 ns window, the cluster is selected as a possible neutron candidate. The number of hits in the 10 ns sliding window is defined as N_{10}^{RAW}, and the earliest timing of the hit in the 10 ns sliding window is defined as t_0. If multiple candidates are found with their t_0 values within 20 ns of each other, only the candidate with the largest N_{10}^{RAW} is considered. If there are two or more candidates which have the same N_{10}^{RAW}, the last one is taken. This procedure avoids double counting the same neutron capture as multiple candidates. The candidate is rejected if N_{10}^{RAW} is larger than 50, or the number of hits in a 200 ns window around the candidate (N_{200}) is larger than 200. The maximum distance of a point in the detector volume to a PMT is 50 meters. Therefore, 200 ns is sufficient to collect most of the photons reaching a PMT without scattering. Accordingly, N_{200} is a good variable to roughly estimate the total visible energy in the detector.

Scintillation from radioactivity in the PMT glass creates a time-clustered noise signal, which can potentially increase the number of observed hits as described in section A. Such spurious hits are removed using the variable, N_{10}, which is similar to N_{10}^{RAW}. Here, N_{10} is the maximum number of hits in a 10 ns sliding window around the 2.2 MeV γ candidate after removing the time-clustered noise hits. In order to eliminate the time-clustered noise, hits are removed when there are multiple hits from the same PMT within 12 µs when N_{10}^{RAW} is smaller than 7, and when there are multiple hits from the same PMT within 6 µs otherwise. A hit cluster, with N_{10} 5 or greater, is regarded as a neutron candidate. Figure 5 shows the distributions of N_{10}^{RAW} and N_{10} for the neutron signal and the background from the simulation. Removing noise hits is shown to be effective in reducing background clusters without a significant loss of signal clusters.

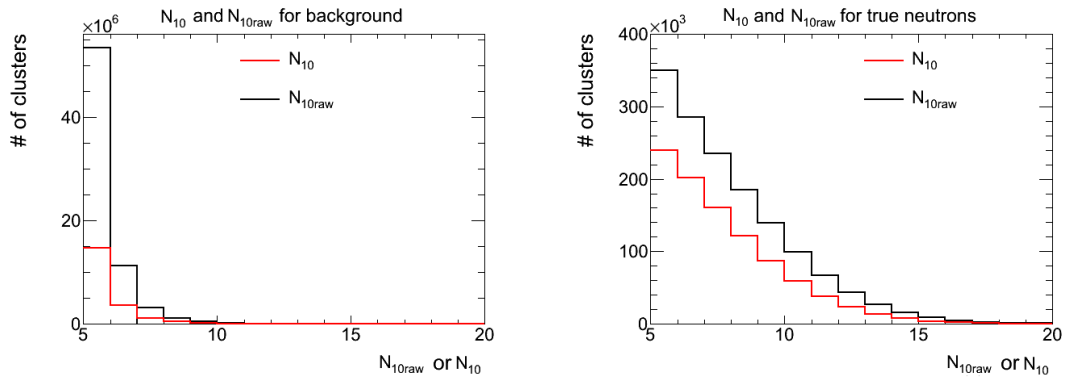

(a) (b)

Figure 5. Distributions of N_{10}^{RAW} and N_{10} (see text for definitions) for background clusters (left) and true neutron clusters (right). Both histograms were made using the same number of primary atmospheric neutrino MC events.

In order to evaluate the efficiency and background rate of the neutron tagging method using the MC sample, the time difference between the t_0 obtained from the neutron tagging algorithm and the true capture time of the neutron is used. If the time difference is less than 100 ns, the candidate

2022 JINST 17 P10029

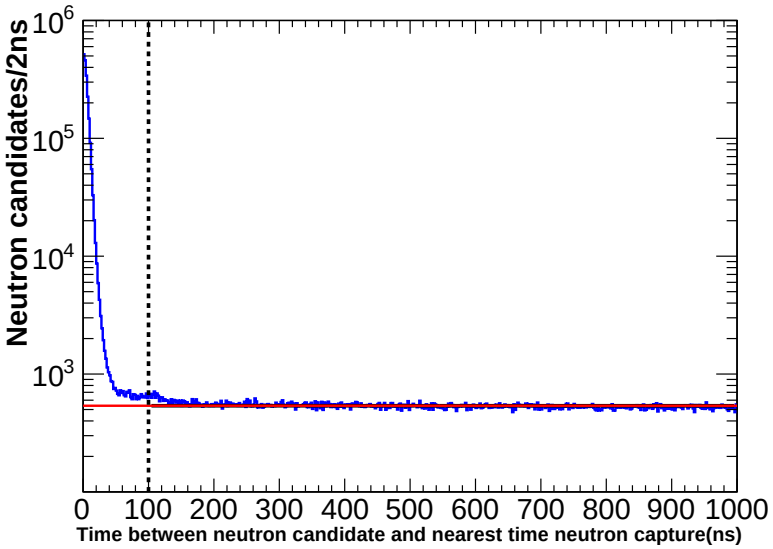

Figure 6. Absolute time difference between neutron candidates and the nearest true neutron capture in MC. The flat tail is assumed to be the background candidate event rate, the spike above the background rate near zero is from true neutron candidates. The dotted black line represents the cut dividing true neutron candidates from fake neutron candidates.

is labeled as correctly-tagged, otherwise, it is labeled as fake. Figure 6 shows the absolute time difference between each neutron candidate and the nearest true neutron capture in the MC. The flat tail is used to estimate the background rate of fake candidates, while the excess on top of this flat rate corresponds to true neutron candidates. By extrapolating the stable background rate into the region around zero where the true neutron candidates appear, it is estimated that about 1.3% of neutrons labeled in MC truth as true candidates are in fact fake, while 0.07% of true neutron candidates are labeled in MC truth as fake. Based on MC truth, the simulation indicates an efficiency of 49% for the candidate selection with a background rate of 22% fake candidates per event.

4.2 Step two: final candidate selection with neural network

Following the initial candidate selection, a neural network is used to separate the neutron capture signal from various backgrounds. In the field of particle physics, neural networks are commonly used as a tool for signal-background classification, and in this analysis, TMulitLayerPerception(TMLP) library in ROOT software framework [25] is used to implement a feed-forward Multi-Layer Perceptron (MLP). In total, twenty-three variables are used as the inputs to the neural network. The neural network was trained on a 250-year-equivalent atmospheric neutrino MC using the MLP method. A separate statistically independent 250-year-equivalent MC data set is then used for testing the trained neural network. After the initial candidate selection process, there are about 1.7 million true neutron candidates, and about 15 million background candidates in the full atmospheric neutrino MC.

Neutrons are typically captured within a few meters of the primary neutrino vertex and a 2.2 MeV γ ray is emitted if proton captures a neutron. The 2.2 MeV γ signal produces $\sim$ 7 PMT hits

2022 JINST 17 P10029

with a timing distribution whose width is typically less than 10 ns after applying the ToF correction. In SK, Cherenkov photons from highly relativistic particles are emitted on a cone with a 42 degree opening angle with respect to the direction of the incident particle, while the azimuthal distribution is uniform as shown in figure 7

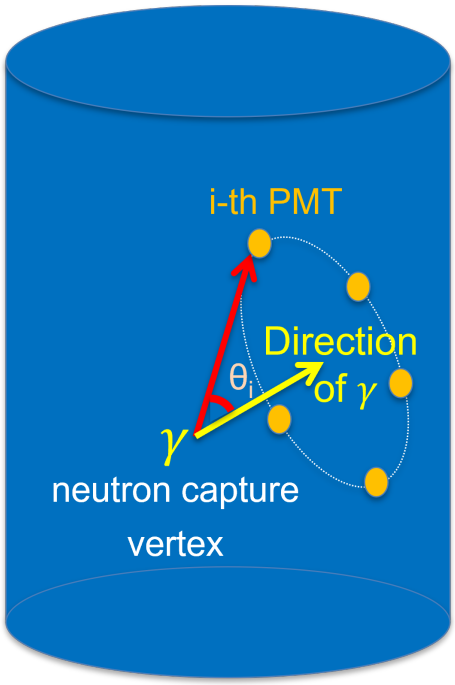

Figure 7. Image of Cherenkov photon emission from a 2.2 MeV γ. The yellow line shows the direction of γ, whose starting point is the neutron capture vertex, the orange filled circles show the hit PMTs, the red line shows the direction to the i-th PMT viewed from the neutron capture vertex, and θ_i is the angle between the γ direction and the direction to the i-th PMT (opening angle), respectively.

Based on these general characteristics we have selected 23 variables to distinguish neutron-induced signals from backgrounds as summarized in table 2.

These variables are classified into three categories, those related to the timing distribution of the PMT hits, those related to the spatial distribution of the hits, and those related to the reconstructed event's vertex and energy.

The variables related to the timing distribution of the PMT hits are: the number of hits in 10 ns after ToF correction (N_{10}), the number of hits in 300 ns without ToF correction (N_{300}), the root-mean-square of hit timing after ToF correction (t_{rms}), the minimum root-mean-square of the hit timing distribution after ToF correction (min(t_{rms})), the difference of N_{10} using the reconstructed primary neutrino interaction vertex and the neutron vertex (ΔN_{10}), and the difference of t_{rms} using the reconstructed primary neutrino interaction vertex and the neutron vertex (Δt_{rms}).

Variables that describe the event topology, such as the spatial charge distribution are: the mean opening angle (θ_{mean}) of PMT hits, the root-mean-square of the azimuthal angle (ϕ_{rms}) of the PMT hits, the number of clustered hits (N_{c}), the acceptance parameter ($P_{\mathrm{Acceptance}}$), the Cherenkov angle likelihood parameter ($L_{\mathrm{Cherenkov}}$), the isotropy parameter (β_l), and the number of hits on low-probability PMTs (N_{low}).

2022 JINST 17 P10029

Finally, variables related to the event reconstruction are: the reconstructed energy using the BONSAI fitter [26] (BS_{energy}), the reconstructed neutron capture vertex position using BONSAI (BS_{wall}), the reconstructed neutron capture vertex position using the Neut-Fit fitter NF_{wall}, the distance from the reconstructed primary neutrino interaction vertex and the reconstructed neutron capture vertex ($(NF-AP)_{\mathrm{dis}}$), the agreement of the reconstructed neutron capture positions of the two different reconstruction algorithms ($(NF-BS)_{\mathrm{dis}}$), and the vertex distance to the ID wall (L_{towall}). Details of the two vertex fitters, BONSAI and Neut-Fit, are described in section B.

Among the input parameters, N_{10} and N_c have the first and the second most significant correlation to the Neural Net output.

Table 2. List of neural net input variables.

Timing distribution of the PMT hits related parameters	
N_{10}	the number of hits in 10 ns after ToF correction
N_{300}	the number of hits in 300 ns without ToF correction
t_{rms}	the root-mean-square of hit timing after ToF correction
$\min(t_{\mathrm{rms}})$	the minimum root-mean-square of the hit timing distribution after ToF correction
ΔN_{10}	the difference of N_{10} using the reconstructed primary neutrino interaction vertex and the neutron vertex
Δt_{rms}	the difference of t_{rms} using the reconstructed primary neutrino interaction vertex and the neutron vertex
Event topology related parameters	
θ_{mean}	the mean opening angle of PMT hits
ϕ_{rms}	the root-mean-square of the azimuthal angle of PMT hits
N_{c}	the number of clustered hits
$P_{\mathrm{Acceptance}}$	the acceptance parameter
$L_{\mathrm{Cherenkov}}$	the Cherenkov angle likelihood parameter
β_l	the isotropy parameter
N_{low}	the number of hits on low-probability PMTs
Event reconstruction related parameters	
BS_{energy}	the reconstructed energy using the BONSAI fitter
BS_{wall}	the reconstructed neutron capture vertex position using BONSAI fitter
NF_{wall}	the reconstructed neutron capture vertex position using the Neut-Fit fitter
$(NF-AP)_{\mathrm{dis}}$	the distance from the reconstructed primary neutrino interaction vertex and the reconstructed neutron capture vertex
$(NF-BS)_{\mathrm{dis}}$	the agreement of the reconstructed neutron capture positions of the two different reconstruction algorithms
L_{towall}	the vertex distance to the ID wall

2022 JINST 17 P10029

In the following subsections all neural network input variables are reviewed. Comparisons of data and the Monte-Carlo simulation for each variable are summarized in section C.

4.2.1 Number of hits in 10 ns: N_{10}

This is the same variable which is used to search for the initial candidates of the 2.2 MeV γ cluster. As above, N_{10} is the maximum number of hits in a 10 ns sliding window around the 2.2 MeV γ candidate after the time-clustered noise cuts. The signal events tend to give larger N_{10} compared to the background as shown in the left plot of figure 20.

4.2.2 Number of hits in 300 ns: N_{300}

Cherenkov photons from a true neutron capture are almost completely contained in a 10 ns window in residual time. However, a fake peak could be detected if there are a sufficient number of Cherenkov photons emitted from a higher energy particle at a different vertex (as explained in figure 8). Therefore, if there is a coincident higher energy event the reconstructed vertex may not be correct.

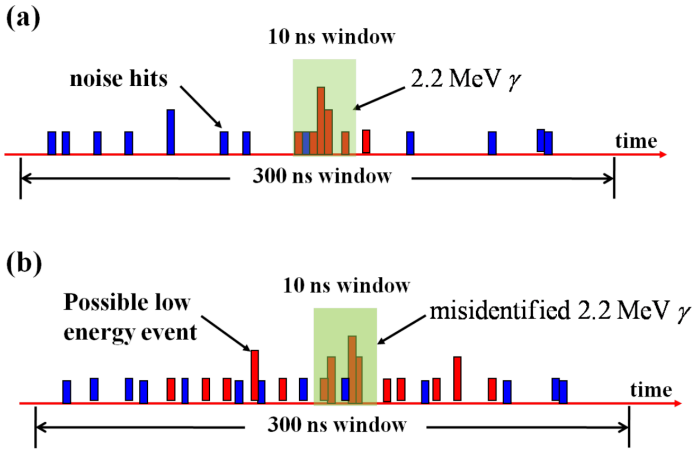

Figure 8. The usefulness of the N_{300} cut: (a) shows a typical neutron capture event and (b) shows a hypothetical background signal to be rejected. The blue bars show dark noise hits and the red bars show the hits from Cherenkov photons.

Considering the size of the detector and the effect of the 'incorrect' ToF subtraction, we have decided to use 300 ns as the timing window for this variable. In order to reject these fake candidates, N_{300} is defined as the total number of hits in a $\pm$150 ns window around the candidate peak. Then, the variable $N_{300} - N_{10}$ is used as an input for the neural network because N_{10} is expected to have a larger fraction of N_{300} for the signal compared to the background, as shown in the right plot of figure 20.

4.2.3 Root-mean-square of hit timing: t_{rms}

The residual timing distribution is expected to have a narrower peak for signal events than for background events. Therefore, the root-mean-square of the candidate hit timing, which is defined in equation (B.1), is selected as one of the neural network input variables. In order to obtain the ToF-corrected timing, we used the reconstructed vertex obtained by the Neut-Fit. The signal events tend to give smaller $\min(t_{\mathrm{rms}})$ compared to the background as shown in the top plot of figure 21.

2022 JINST 17 P10029

4.2.4 Minimum root-mean-square of hit timing: $min(t_{\mathrm{rms}})$

Background PMT hits can sometimes occur in the 10 ns residual time window along with the hits from a true neutron capture. For further reduction of these background hits, the RMS of the hit timings is calculated for every set of three consecutive hits in the 10 ns window, as shown in figure 9). Here, the Neut-Fit vertex is used to correct for the ToF.

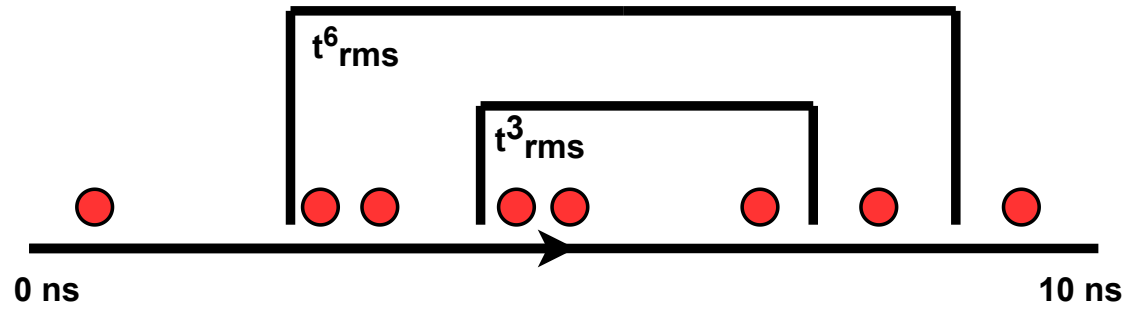

Figure 9. The selection of $min(t_{\mathrm{rms}})$ hit clusters. Optimal selections for clusters of 3–6 hits are shown for an example candidate where $N_{10} = 8$. Possible background hits on the fringes of the candidate time are ignored.

The smallest value of all the sets is passed on as $\min(t^3_{\mathrm{rms}})$. A similar quantity is also calculated for sets of six hits and defined as $\min(t^6_{\mathrm{rms}})$ and these two variables are used as the neural network inputs. The hits from the signal are expected to be concentrated in time, and thus these variables are smaller for the signal compared to the background, as shown in the bottom plots of figure 21.

4.2.5 Neut-fit root-mean-square of hit timing variable and number of hits in 10 ns: Δt_{rms}, ΔN_{10}

The variable t_{rms} is calculated twice, once with the hits which are ToF-corrected to the primary event vertex, and again with the hits which are ToF-corrected to the Neut-Fit vertex. The difference between the two t_{rms} values is defined as Δt_{rms}, and is used in the neural network. Note that when t_{rms} is recalculated using the Neut-Fit vertex, additional hits can be moved into the 10 ns window and can have the effect of increasing t_{rms}. This means that sometimes Δt_{rms} can be negative. Instead of using the reconstructed vertex from APFit, N_{10n} is defined as the value of N_{10} recalculated using the vertex from Neut-Fit. The difference, ΔN_{10}, is defined as $N_{10n} - N_{10}$. These two variables are expected to be close to 0 for the signal because the vertexes between the two reconstructions are expected to be close for signal but not necessarily same for the background, as shown in figure 22.

4.2.6 Mean opening angle: θ_{mean}

In water, Cherenkov photons from highly relativistic particles are emitted on a cone with a 42 degrees opening angle with respect to the direction of the incident particle. Therefore, Cherenkov photons from electrons that are Compton-scattered by a 2.2 MeV γ are expected to have a peak opening angle around 42 degrees. In contrast, background candidates are not expected to form such a peak. The direction of the Compton-scattered electron is reconstructed as the vector sum of the directions from the Neut-Fit vertex to each PMT hit in the 10 ns window. Here, the timing of each hit is ToF-corrected using the Neut-Fit vertex, and the opening angle to each hit PMT is then calculated from this direction. The mean value of these angles is used as an input variable. The top left plot of

2022 JINST 17 P10029

figure 23 shows distributions of the mean opening angles for the signal and the background; a clear peak around 42 degrees is observed for the signal.

4.2.7 Hit vector root-mean-square of the azimuthal angle: ϕ_{rms}

Cherenkov hits from a true neutron capture are expected to be distributed uniformly in the azimuth of the reconstructed direction of the Compton-scattered electron. Background candidates, on the other hand, are often geometrically concentrated and form compact clusters of hits. The variable ϕ_{rms} is computed by calculating the azimuthal angle of each hit with respect to the reconstructed direction of the Compton-scattered electron, where the definition of the direction is same as the one used to calculate θ_{mean}. Angles between consecutive hits in the azimuth are then calculated such that the variable ϕ_{rms} is the root-mean-square of these angular differences. This variable is expected to be small for a true neutron capture, since the steps between consecutive hits are fairly uniform. For background events with spatial clusters, this variable is larger, since the steps are small when stepping through hits in a spatial cluster and then become larger when moving away from the cluster to other hits in the event. The top right plot of figure 23 shows the signal and the background distributions for ϕ_{rms}.

4.2.8 Number of clustered hits: N_{c}

Background candidates are often found to have geometrically-clustered PMT hits. Radioactive contaminants in the PMT glass could be the source of these backgrounds, and since radioactive products emit weak Cherenkov light, they may be detected by nearby PMTs. Conversely, because the primary event vertex is required to be at least 200 cm from the wall, hits from a true neutron capture are not expected to be clustered tightly together. This clustering tendency can thus be used to separate the signal from the background.

Clusters are defined based on the opening angles between hits, viewed from the Neut-Fit reconstructed vertex. Clusters are built starting with a single hit and hits are then added to the cluster iteratively according to the following rule: if a hit is within 14.1 degrees of any hit in a cluster, it is added to the cluster. The number of clustered hits, N_c, is defined as the total number of hits in clusters of 3 or more hits.

The neural network uses $N_{10} - N_{\mathrm{c}}$ as an input variable. Since the spatial distribution of PMTs for signal events is expected to be broad, N_{10} is much larger than N_c. On the other hand, $N_{10} - N_{\mathrm{c}}$ is expected to be small for background events, as shown in figure 23.

4.2.9 Acceptance parameter: $P_{\mathrm{Acceptance}}$

The probability to detect photons from a signal γ depends on the position of the PMT and its relative orientation to the incoming photon. Most noise hits on the other hand do not have this dependency. Therefore, it is possible to discriminate the signal from noise using this difference. First, we define the probability P_i for each PMT to detect Cherenkov photons using the distance from the neutron capture position to the PMT and the direction. Then, the acceptance parameter, $P_{\mathrm{Acceptance}}$, is obtained by multiplying the probability P_i for all the PMTs used to calculate N_{10}. Here P_i and

2022 JINST 17 P10029

$P_{\text{Acceptance}}$ are defined as follows:

$$A_i = \frac{F(\theta_i)}{R_i^2} e^{-R_i/L}, \tag{4.1}$$

$$A_{\text{Total}} = \sum_i A_i, \tag{4.2}$$

$$P_i = \frac{A_i}{A_{\text{Total}}} \tag{4.3}$$

$$P_{\text{Acceptance}} = \frac{\log(\prod_i^{N_{10n}} P_i)}{N_{10n}}, \tag{4.4}$$

where $F(\theta_i)$ encodes the angular dependence of the PMT detection efficiency, R_i is the distance from the captured neutron position to the i-th PMT, and L is the light attenuation length in water. The Neut-Fit vertex is used in the calculation of distance (R_i) and angle θ_i.

Acceptance values for signal neutron events are expected to be larger compared to those for the backgrounds, as is shown in the left plot of figure 24.

4.2.10 Cherenkov angle likelihood parameter: $L_{\text{Cherenkov}}$

Signal photons are expected to be distributed near 42 degrees from the direction of the relativistic electron that produced them. In order to quantify this characteristic, a Cherenkov angle likelihood parameter ($L_{\text{Cherenkov}}$) is defined as follows. First, cones are defined using combinations of three PMT positions from N_{10n} to specify a base, and the Neut-Fit vertex is used for the apex. The opening angle of a given cone is defined as θ_i for the i-th PMT combination. The likelihood functions L_{bkg} and L_{sig} are constructed as functions of θ_i, N_{10n} and the products of probabilities defined in equation (4.3) for those three hits ($\prod_{j=1}^{3} P_j$). Then the Cherenkov angle likelihood parameter ($L_{\text{Cherenkov}}$) is defined as:

$$L_{\text{Cherenkov}} = \sum_{i=0}^{{}^{N_{10n}}\text{C}_3} (\log(L_{\text{bkg}}(N_{10n}, \theta_i, \prod_{j=1}^{3} P_j)) - \log(L_{\text{sig}}(N_{10n}, \theta_i, \prod_{j=1}^{3} P_j))). \tag{4.5}$$

The distribution of this likelihood parameter for the signal and the background is shown in figure 24, where the values for the signal events are clearly smaller compared to the ones for the background events.

4.2.11 Isotropy parameter: β_l

Isotropy parameters are introduced to characterize the spatial distribution of the detected photons. First, β_l is defined as follows:

$$\beta_l = \frac{2}{N_{10n}(N_{10n}-1)} \sum_{i=1}^{N_{10n}-1} \sum_{j=i+1}^{N_{10n}} P_l(\cos\theta_{ij}), \tag{4.6}$$

where θ_{ij} is the opening angle between two PMTs with hits as viewed from the reconstructed neutron vertex with Neut-Fit. Here l is a natural number which has been chosen to be smaller than 6 in this analysis and P_l is formed from spherical harmonics. These β parameters are constructed as follows.

2022 JINST 17 P10029

At first, we define a function $f(\theta, \phi)$, which gives 1 when there is a PMT which has detected a photon and gives 0 otherwise. Here, θ and ϕ are zenith and azimuthal angles of the PMT viewed from the Neut-Fit vertex. The $f(\theta, \phi)$ is expressed using the spherical harmonic function $Y^*_{lm}(\theta, \phi)$,

$$f(\theta, \phi) = \sum_{l=0}^{\infty} \sum_{m=-l}^{l} \alpha_{lm} Y^*_{lm}(\theta, \phi). \tag{4.7}$$

Here we define the position of i-th hit PMT as (θ_i, ϕ_i), then α_{lm} is

$$\alpha_{lm} = \int \int f(\theta, \phi) Y_{lm}(\theta, \phi) d\theta d\phi \tag{4.8}$$

$$= \sum_{i=1}^{N_{10n}} Y_{lm}(\theta_i, \phi_i). \tag{4.9}$$

Next we define the rotationally invariant variable β'_l,

$$\beta'_l = \sum_m |\alpha_{lm}|^2 \tag{4.10}$$

$$= \sum_{i,j} \sum_m Y_{lm}(\theta_i, \phi_i) Y^*_{lm}(\theta_j, \phi_j) \tag{4.11}$$

$$= \frac{2l+1}{4\pi} \sum_{i,j} P_l(cos\theta_{ij}). \tag{4.12}$$

β'_l depends on the number of PMT hits and also, same combinations of PMTs are used multiple times. Therefore, we use β_l, which is defined as shown in equation (4.6), instead of β'_l.

The distributions of β_l used in the neural network are shown in figure 25. As shown in these figures, the signal events concentrate around 0.35 for β_1 and around 0 for other values of l, while backgrounds have broader distributions and have peaks at around 1.

4.2.12 Alternative fit variables: BS_{wall}, NF_{wall} and BS_{energy}

It is known that Radon emanates from the SK detector components, in particular the PMTs, their signal and HV cables, and the anti-implosion PMT housings. The subsequent decay of Radon produces background events concentrated near these materials and hence close to the inner detector wall. Therefore, the distance between the neutron vertexes reconstructed by alternative event reconstruction tools and the nearest inner detector wall is selected to separate the signal from the background. We have used two event reconstruction tools, BONSAI and Neut-Fit. The variables BS_{wall} and NF_{wall} are calculated using BONSAI and Neut-Fit, respectively and the distributions are shown in the top plots of figure 26. BONSAI also gives the reconstructed energy and this variable (BS_{energy}) is expected to be around 2.2 MeV for true neutron captures. Therefore, this variable is also used as one of the inputs. The bottom plot of figure 26 shows the distribution of BS_{energy} there is a clear peak at 2.2 MeV for signal but much broader distribution for background.

4.2.13 Fit agreement variables: $(NF - BS)_{\text{dis}}$, $(NF - AP)_{\text{dis}}$

Neut-Fit and BONSAI use different fit criteria and procedures to search for low energy event vertexes. When they agree well on the location of an event, it is likely to be a real low energy event, as opposed

2022 JINST 17 P10029

to simply PMT noise. Therefore, the distance between these two vertexes $(NF - BS)_{\mathrm{dis}}$ is also selected as an input to the neural network and the distribution is shown as the left plot of figure 27. Furthermore, neutrons are expected to travel no further than a few meters from their production points before thermalizing and being captured, as shown in the right plot of figure 27. Therefore, the distance between the Neut-Fit neutron vertex and APFit primary vertex, $(NF - AP)_{\mathrm{dis}}$ is also used as an input to the neural network.

4.2.14 Distance to the ID wall parameter: L_{towall}

We define the distance from Neut-Fit's reconstructed neutron vertex to the ID wall in the direction of the particle as "to wall" (L_{towall}). The direction of the particle is defined by the sum of the vectors from the reconstructed neutron vertex to each hit PMT. The distribution of L_{towall} is shown in figure 28. As shown in the figure, the noise distribution has a larger mean value compared to the signal.

4.3 Neural network results

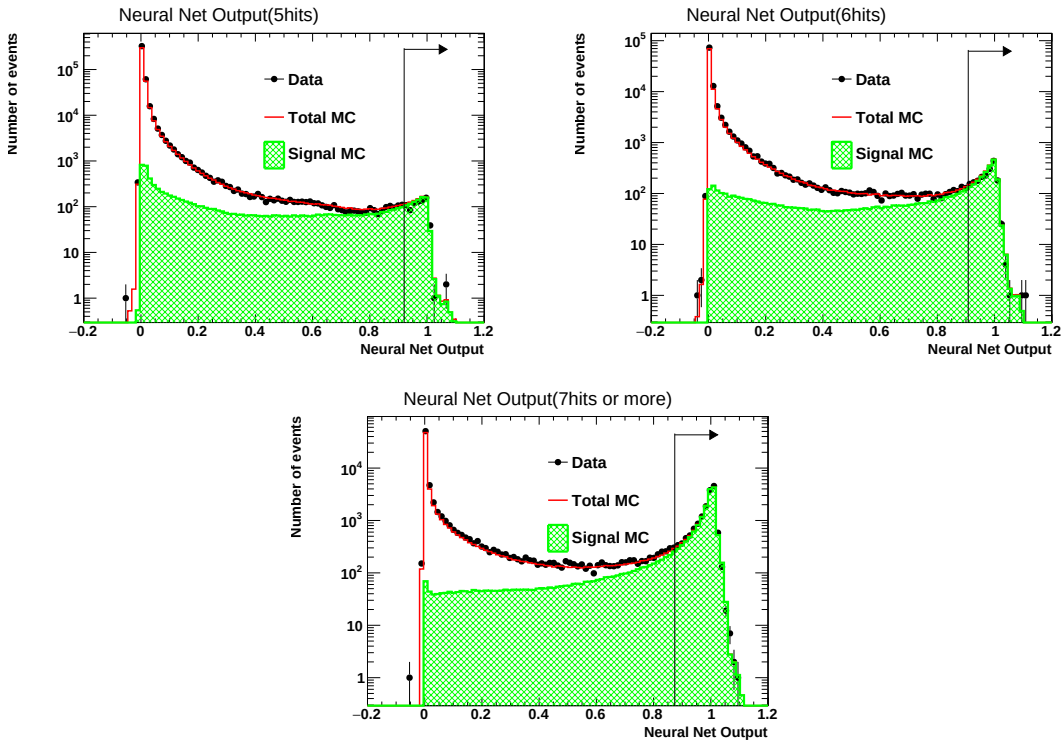

Figure 10. Neural network output for selecting final neutron candidates. The plots show the output for different values of N_{10}: 5 in the top left panel, 6 in the top right, and 7 or more in the bottom panel. The green histogram corresponds to the neutron capture signal, the red histogram shows the total MC, and the overlaid black points show the data, respectively. The red histogram is normalized to the number of neutron capture events in the atmospheric neutrino event samples from the full SK-IV data set, which spanned 3,244.4 days between October 2008 and May 2018. Black lines and arrows in each plot show the threshold values for selecting candidates. Since noise contamination is larger for small N_{10} candidates, different threshold values were chosen to ensure the mis-identification rate is below 0.018 per neutrino interaction. The threshold values are 0.92 when N_{10} is 5, 0.908 when it is 6, and is 0.874 for 7 or more.

The output of the neural network is shown in figure 10 and is defined such that it is approximately equal to the likelihood of that candidate being a true neutron capture. The neural network successfully separates the true neutron candidates from the fake neutron candidates. As described above, a neutron candidate is identified as a "true candidate" if the time difference between it and the true capture time of an MC neutron is less than 100 ns. Threshold values for selecting neutron candidates are chosen such that the mis-identification of noise events is less than 0.018 per neutrino interaction. Since the fraction of noise events increases dramatically when N_{10} decreases, the chosen thresholds vary based on this parameter. The thresholds are 0.92 for $N_{10} = 5$, 0.908 for $N_{10} = 6$ and 0.874 when $N_{10} > 6$. When applied to the 500 year atmospheric neutrino MC data, these cut values give a final neutron tagging efficiency of 26% with 0.016 background neutron tags per primary event as shown in table 3. Here, there are sufficient MC statistics to make statistical error negligibly small.

Table 3. Final efficiency and background rate of the neutron tag algorithm after each stage of the selection.

Selection stage	Efficiency	Background / Event
Initial Selection	49%	22
After Neural Network	26%	0.016

The efficiency is heavily dependent on the distance between the neutrino interaction and the neutron vertex and is mildly dependent on the energy deposited in the detector, as shown in the top two plots in figure 11. Here, the total energy deposit in the detector is defined as the electron-equivalent energy (E_{vis}). It also depends on the vertex position of the primary event in the detector. If the primary event is close to the center of the tank, the attenuation in the water reduces the amount of light reaching the PMTs and the detection efficiency decreases. However, if the event is too close to the tank wall, the PMT acceptance is reduced and the efficiency also decreases. As shown in the bottom plot in figure 11, the efficiency is maximal for events in the region between the center and edge of the fiducial volume.

5 Comparison with SK-IV data

The neutron tagging algorithm was applied to 3,244.4 days of SK-IV FC data and compared to a 250 years sample of atmospheric neutrino MC data, which included oscillations. This SK-IV data set corresponds to 26,473 FC events whose reconstructed vertexes are at least 200 cm from the ID wall. The details of the atmospheric neutrino event selection are discussed in a previous article [2]. The MC sample is livetime-normalized and oscillated using a two-flavor oscillation approximation with $\Delta m^2 = 2.5 \times 10^{-3}\,\mathrm{eV}^2$ and $\sin^2 2\theta = 1.0$. A summary of the comparison is shown in table 4. The agreement between the observed number of atmospheric neutrino events and the MC prediction without any corrections is typically within ~5%. In other analyses at SK, nuisance parameters modeling flux or neutrino interaction uncertainties are applied to modify the MC expectation to agree with the data. However, the present study does not include these corrections. Note that only events whose electron-equivalent energy (E_{vis}) is smaller than 30 GeV are used here. At higher energies, the flux is highly suppressed and neutrino interactions have a large neutron multiplicity, which is not modeled well in our Monte-Carlo simulation programs, NEUT and SKDETSIM.

2022 JINST 17 P10029

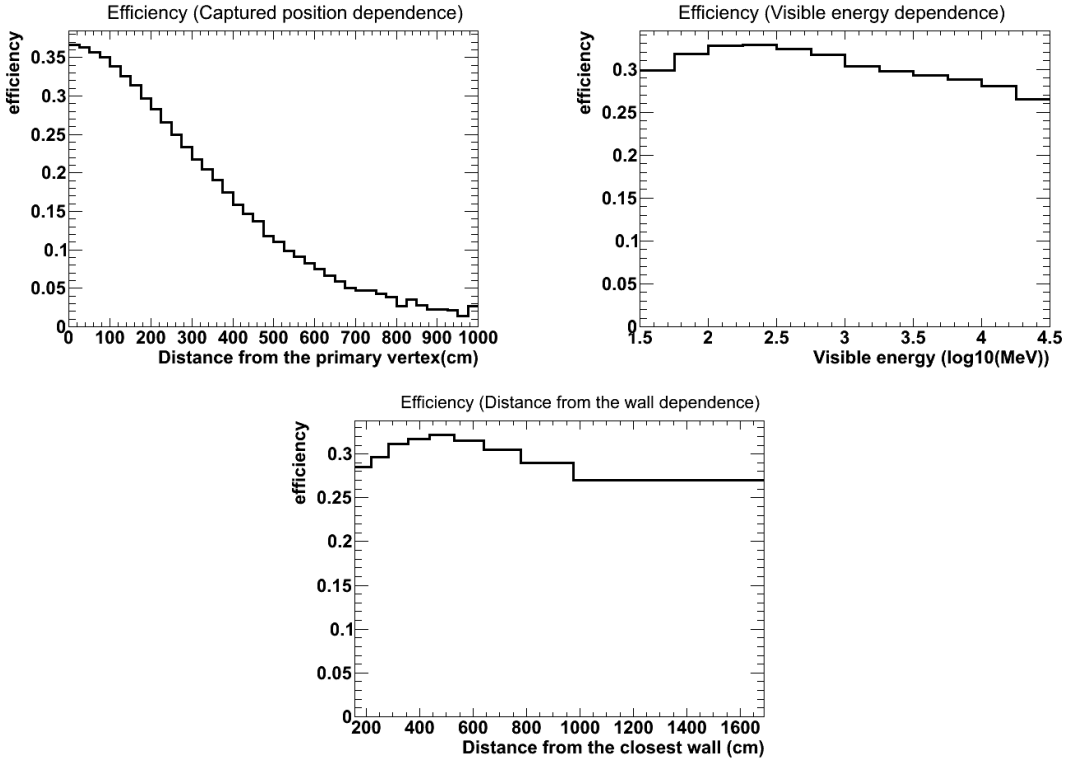

Figure 11. Dependencies of the 2.2 MeV detection efficiency on the distance traveled by the neutron (top left), the visible energy of the primary neutrino interaction (top right) and the efficiency of detecting neutrons as a function of distance from the closest ID wall (bottom). The efficiency is defined as the number of selected candidates divided by the number of true neutron capture events in each bin.

Table 4. A comparison of the expected and measured number of neutron capture events in the SK-IV atmospheric neutrino SK-IV data. The MC data sample is normalized to the data livetime and oscillated under a two-flavor approximation: $\Delta m^2 = 2.5 \times 10^{-3}$ eV^2 and $\sin^2 2\theta = 1.0$.

Sample	SK-IV Data (3,244.4 days)	MC
Fully contained events	26,473	25,845
Total neutrons tagged	18,091	18,288
Events with at least one tagged neutron	9,327	8,912.7
Events with exactly one tagged neutron	5,676	5,138.3

The difference between each tagged neutron's timing and the primary event timing is shown in figure 12. By fitting the data to a falling exponential with a constant offset, a capture lifetime of 218 ± 9 µs was extracted with a χ^2 of 33.1 for 25 degrees of freedom. This is consistent with the previously measured lifetime of 204.8 ± 0.4 µs [8]. By assuming that the falling exponential part of the fit is from true neutrons while the flat constant is from backgrounds, it is estimated that 100% ± 3.23% of tagged neutrons correspond to true neutron captures. Performing the same analysis on MC resulted in 97.9% ± 3.94%, which is consistent with the results from the data. The total number of events with neutrons, the average multiplicity, and the neutron multiplicity subdivided into

2022 JINST 17 P10029

sub-GeV ($E_{\rm vis} < 1,330$ MeV) and multi-GeV ($E_{\rm vis} > 1,330$ MeV) samples are shown in figure 13. These plots are normalized to the data livetime and the MC includes oscillations as described above.

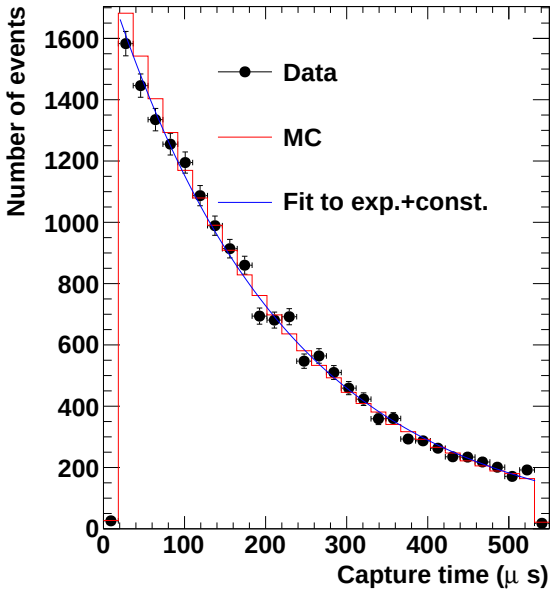

Figure 12. Timing distribution of selected 2.2 MeV γ candidates. The primary trigger is at $t = 0$. The blue curve is the best fit to an exponential function with a constant offset. Data are taken from 3,244.4 days of SK-IV and the MC is normalized as in table 4.

6 Systematic error study using the americium-beryllium source

In order to study the efficiency of neutron tagging with a well-defined control sample, calibration data sets were collected in 2016 by deploying an americium-beryllium (Am-Be) source in the SK detector. The ^{241}Am emits an α-particle which interacts with ^{9}Be and emits a neutron as follows:

$$\alpha + {}^{9}\mathrm{Be} \rightarrow {}^{12}\mathrm{C}^{*} + n \tag{6.1}$$

$$ {}^{12}\mathrm{C}^{*} \rightarrow {}^{12}\mathrm{C} + \gamma\ (4.43\,\mathrm{MeV}) \tag{6.2}$$

or

$$\alpha + {}^{9}\mathrm{Be} \rightarrow {}^{12}\mathrm{C} + n\ (\text{ground state}) \tag{6.3}$$

The intensity of the ^{241}Am source was 97 μCi and the emission rate of 4.43 MeV γ was measured to be 87 Hz. From this measurement the ground state transition rate was estimated to be 76 Hz [9]. As shown in figure 14, the Am-Be source is embedded in a 5 cm cube of bismuth germanium oxide (BGO) scintillator to amplify the light released by the 4.43 MeV γ. This scintillation light is used to trigger the SK detector and initiate a search for a subsequent neutron capture signal. The ground-state transition produces an irreducible constant background of neutrons. Upon triggering, an extended time window of $-5 \rightarrow 835$ μs is stored in order to study the detection efficiency.

2022 JINST 17 P10029

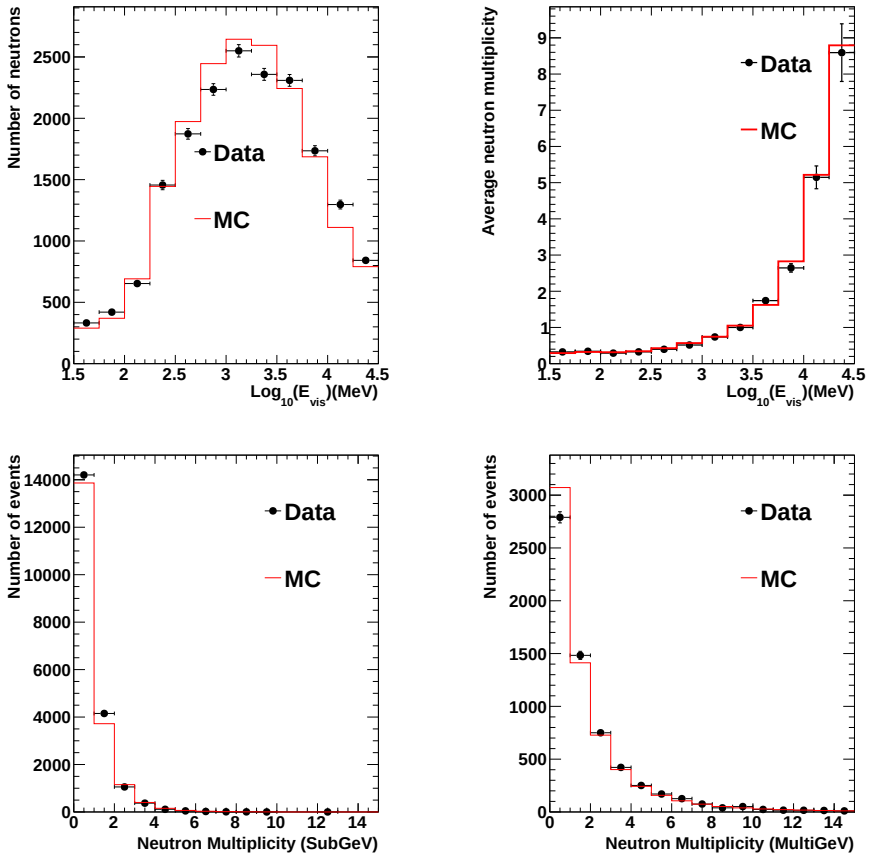

Figure 13. Comparison of data and MC for tagged neutrons in the SK-IV atmospheric neutrino data. The top left (right) plot shows the total number of neutrons (average neutron multiplicity) as a function of visible energy ($E_{\rm vis}$). The bottom left plot shows the neutron multiplicity for sub-GeV events ($E_{\rm vis} < 1.33$ GeV) and the bottom right plot shows that for multi-GeV events ($E_{\rm vis} \geq 1.33$ GeV). These plots are normalized to the number of neutrino events observed in the data. Only statistical errors are shown.

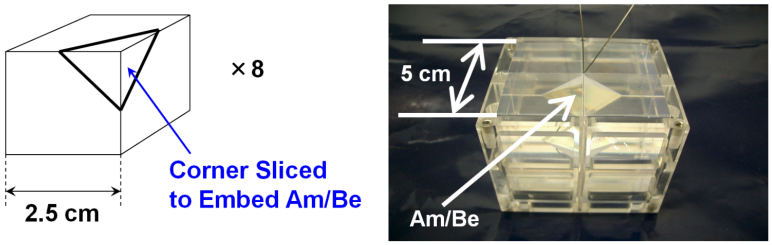

Figure 14. Am-Be crystal embedded in a 5 cm cube of BGO scintillator. This is held in an acrylic case.

The Am-Be source was placed at three different locations in the SK tank: the position called Center is $(35.3, -70.7, 0)$ cm, the position called Y12 is $(35.3, -1201.9, 0)$ cm, which is close to the barrel wall, and the position called Z15 is $(35.3, -70.7, 1500.0)$ cm, which is close to the top of the tank. In order to estimate the accidental background, we have also collected randomly triggered data with this source.

6.1 Am-Be data selection

The primary selection criteria for 4.43 MeV γ events is based on the number of p.e. detected in the ID. The total observed p.e. from the BGO scintillator placed at the center of SK is shown in figure 15. We have studied the shape of the p.e. distribution from the BGO scintillator with a dedicated Monte-Carlo simulation program based on GEANT4. A qualitative study of the simulation results suggested that the interactions of neutrons in the BGO scintillator produce a large number of p.e. and the shape of the tail agrees quite well with the data. The discrepancy between the data and the simulation in the tail region is coming from the uncertainty of the light emission of BGO for neutron. In order to select the prompt events triggered by a 4.43 MeV γ, the selection criteria are defined as follows:

$$\begin{aligned} \text{Center: } & 750 < \text{p.e.} < 1,050 \\ \text{Y12: } & 850 < \text{p.e.} < 1,150 \\ \text{Z15: } & 900 < \text{p.e.} < 1,150. \end{aligned}$$

Since the light attenuation from the source position to the PMTs is different for different source positions, different cut values are used.

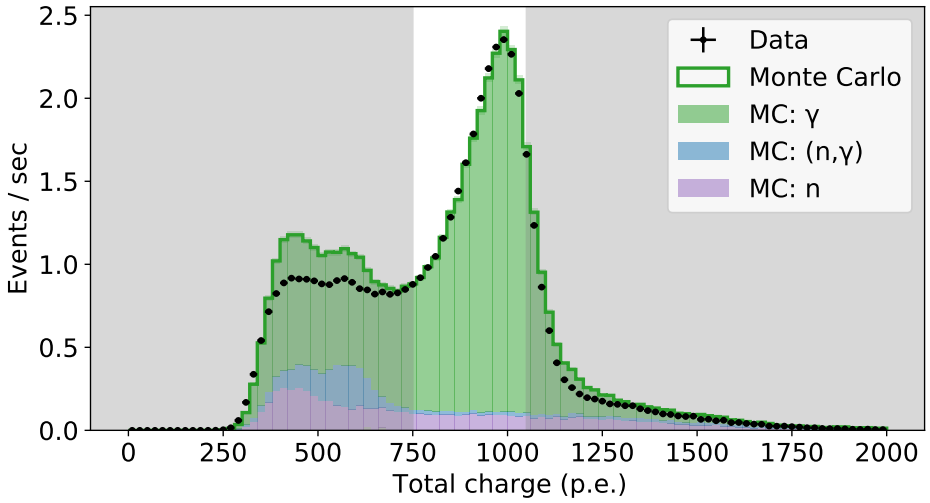

Figure 15. Total photo-electrons from 4.43 MeV γ scintillation events with the Am-Be source positioned at the center of the tank. The black points show the data. The histogram shows the distribution obtained by the Monte-Carlo simulation. The green shaded area corresponds to the events originated by γ, the blue shaded area corresponds to the events originated by neutron and γ, and the purple shaded area corresponds to the events originated by neutron. Events with $750 < \text{p.e.} < 1,050$ were selected to trigger 4.43 MeV γ events. The Monte-Carlo histogram is normalized to the number of events of the data, whose total charge is $750 < \text{p.e.} < 1,050$. The events in the gray shaded area are not used for the analysis.

In addition, the primary 4.43 MeV γ event is required to be at least 1.5 ms later than the previous primary event in order to avoid contamination from prior neutron emissions. A search for delayed activity is then performed using the number of hits in a 200 ns sliding time window (N_{200}). If there

2022 JINST 17 P10029

is a timing cluster whose N_{200} is larger than 49 hits, this event is rejected to eliminate possible contamination from cosmic ray muons or other background sources. In this search, the evaluation of N_{200} starts 200 ns after the primary event, as the BGO crystal scintillator has a long decay component.

6.2 Am-Be data analysis

Neutron tagging is applied to the selected Am-Be events and a corresponding MC sample. Here we use the same neural network trained for the atmospheric neutrino data analysis. Since the kinetic energy is much lower for the neutrons coming from the Am-Be source (from 2 to 10 MeV) compared to the neutrons produced by the atmospheric neutrino interactions, the capture positions of the neutrons are expected to be much closer. Therefore, the location of the source is used as the capture position for the ToF corrections for both real data and MC in the analysis. The other difference is that the total number of photons from the primary 4.43 MeV γ is small so there is no need to take into account the after-pulsing of the PMTs. Also, the gate width for this data is enlarged to 835 µs and the neutron search timing window is accordingly enlarged from 18–535 µs to 10–835 µs. Simulated events are produced by injecting neutrons in the detector with an energy spectrum based on an α-Be capture (equation (6.1) to (6.3)) as given in reference [27].

6.3 Systematic uncertainty evaluation

Systematic uncertainties on the neutrino tagging method are evaluated for the initial and final candidate selection steps independently. Since the first selection uses N_{10} to select candidates, a comparison of the MC and data in this variable is used to estimate the systematic uncertainty. This variable is known to have a strong dependence on the photon detection efficiency of the PMTs, which is the dominant source of the uncertainty. In the error analysis, simulations with different photon detector efficiencies are generated and compared against the background-subtracted N_{10} distribution in the data. Figure 16 shows the N_{10} distributions of the data, together with the true neutron and the background from the MC. Here, random trigger data taken at the same time as the calibration run is used as the background in the MC. The MC has been normalized to the number of events collected with the Am-Be source deployed. These distributions show good agreement indicating the background can be safely subtracted.

The left plot of figure 17 shows the distributions of N_{10} for the background-subtracted data and simulation, with the nominal value used for the photon detection efficiency in the simulation. Fitting this data assuming different detection efficiencies yields the χ^2 distribution shown in the right plot of figure 17. The minimum value of the χ^2 was obtained when the photon detection efficiency is changed by −0.9%. A 2.2% change is allowed at 1σ which corresponds to a 1.7% change in the number of candidates passing the initial selection.

The final event selection is done using the neural network. The systematic uncertainty for this step is evaluated by comparing the relative neutron tagging efficiencies between data and MC for candidates that pass the initial selection. This relative efficiency (ϵ_r) is defined as $\epsilon_r = \epsilon_{\mathrm{NN}}/\epsilon_{\mathrm{IS}}$, where ϵ_{IS} is the efficiency for identifying the neutron using the initial candidate selection and ϵ_{NN} is the efficiency for identifying the neutron using the neural network selection. Before estimating the efficiencies, we checked whether the neutron tagging algorithm is working properly with the Am-Be data. For this purpose, the neutron capture time was fitted using the initial candidates and those

2022 JINST 17 P10029

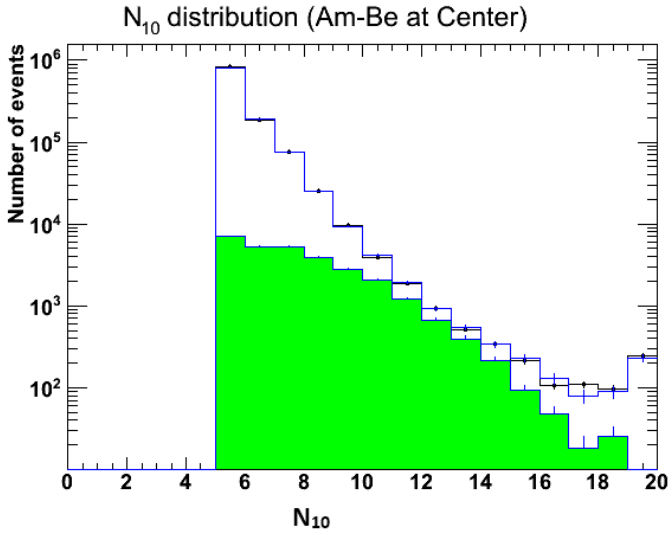

Figure 16. N_{10} after the initial selection of the Am-Be calibration data. The green histogram shows the true neutron in the MC, the blue histogram shows the sum of the true neutrons and background in the MC, and the black filled circles with error bars show the data. The blue histogram has been normalized to the number of real data events. The last bin contains the overflow events.

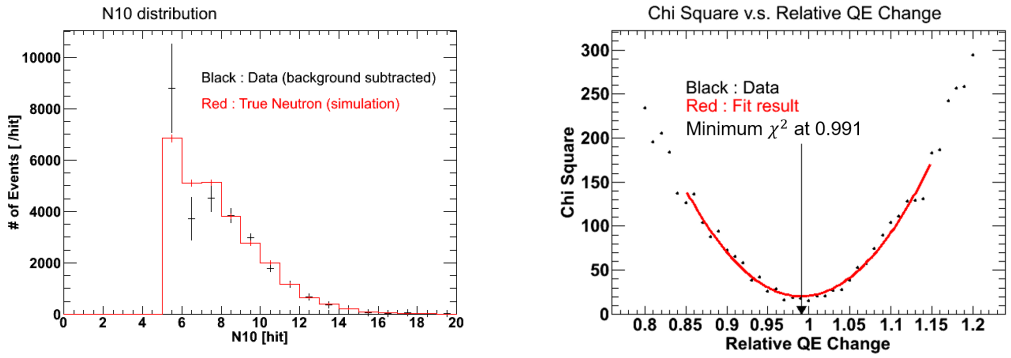

Figure 17. The N_{10} distribution after the initial selection (left). Black points show the data after background subtraction and the red histogram shows the true neutron distribution from the Monte-Carlo simulation. The photon collection efficiency is set to its nominal value in this figure. The χ^2 distribution from a fit to the data as a function of the simulated photon detection efficiency (right). Black points show the data and the red line shows the result of a fit with a parabolic function.

passing the neural network. Figure 18 shows the distribution of the neutron capture times. All the obtained capture times are close to 200 µs, which are consistent with the past measurements.

Using three data samples taken at the three different Am-Be positions, Center, Z15, and Y12, the efficiencies of the initial selection ϵ_{IS} and ϵ_{NN} are calculated for both data and MC sample. The obtained ϵ_r values for the data and the MC sample are summarized in table 5 and the maximum efficiency difference is 8.8%.

In summary, there is a 1.7% uncertainty in the initial selection and an 8.8% uncertainty in the neural network selection. Therefore, we assign ±9.0% as the neutron detection uncertainty.

2022 JINST 17 P10029

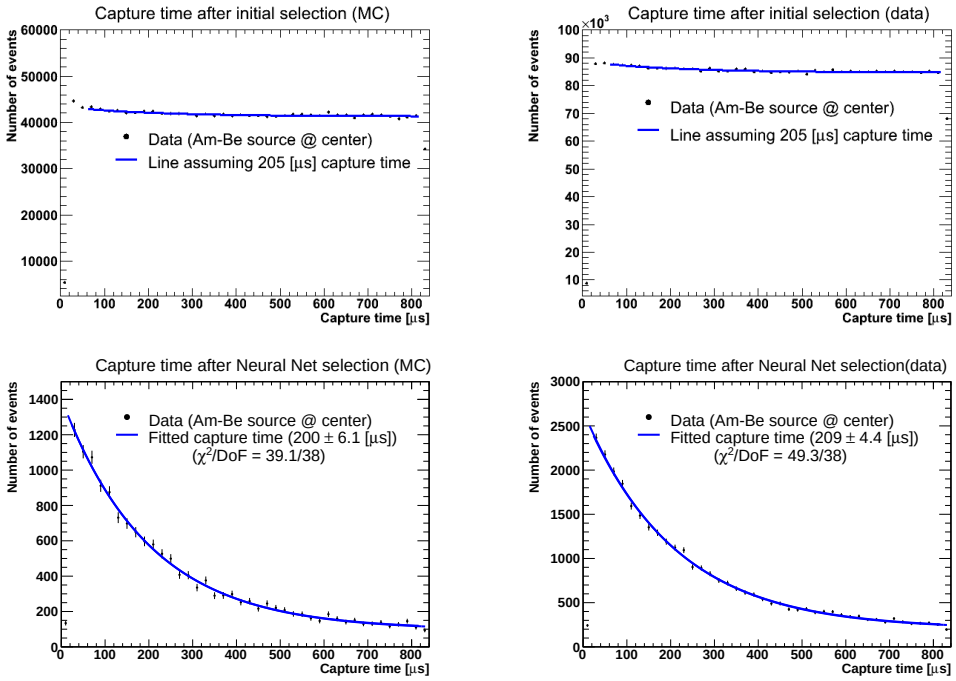

Figure 18. Neutron capture times for data and MC with the Am-Be source. The upper two figures show the capture time for events passing the initial selection. The bottom two figures show the capture time after the neural net selection. Black dots show the data while the blue lines in the upper two plots are reference lines assuming a capture time of 205 μs. Blue lines in the lower two plots show the results of fits for the neutron capture time.

Table 5. Relative neutron tagging efficiencies ($\epsilon_{NN}/\epsilon_{IS}$) in percent obtained for the Am-Be sample.

	Data	MC data	(MC - Data)/Data
Center	62.7%	60.0%	−4.5%
Z15	62.5%	67.0%	8.8%
Y12	68.1%	65.9%	−3.2%

7 Conclusion

A new neutron tagging technique has been developed for identifying neutrons produced in the atmospheric neutrino data sample of Super-Kamiokande-IV. A tagging efficiency of 26%, with the accidental background rate of 0.016 per neutrino event, has been achieved. The error of the tagging efficiency is estimated to be 9.0%. This method was verified with an americium-beryllium neutron source. Discrepancies of up to ∼ 10% in the detection efficiencies of data and MC samples were observed. These discrepancies seem to arise from assumptions made in the production of the Monte-Carlo simulation and from the uncertainties in the modeling of the americium-beryllium neutron source itself. This neutron tagging method was applied to 3,244.4 days of SK-IV data and 18,091 neutron-capture candidates were identified. This agrees well with MC predictions. Using the detected neutron candidates, the neutron capture livetime in water was measured to be 218 ± 9 μs.

2022 JINST 17 P10029

This technique provides the ability to utilize additional information in neutrino interactions. Measuring neutron multiplicity in an event is expected to improve the separation of anti-neutrino events from neutrino events and improve the background rejection in nucleon decay analyses. Although neutron information plays a crucial role in various physics studies, it is difficult to improve the efficiency much further due to the limited number of photons emitted from the scattering of the 2.2 MeV γ from neutron capture in water. Therefore, the SK collaboration has started to dissolve gadolinium into the water since it captures neutrons efficiently and emits several MeV in multiple γ rays. This will enable more efficient neutron tagging and improve the capability of the SK experiment [6].

A Noise characteristics of the 20-inch PMT

The typical noise rate of a 20-inch PMT in SK is around 5 kHz at a 0.25 photo-electron (p.e.) threshold. A careful study of the noise revealed that it consists of two components. The first component is distributed uniformly in time while the other forms clusters in time. The timing distribution of repeated hits following a signal pulse above the discriminator threshold (~ 0.25 p.e.) of a 20-inch PMT is shown in figure 19. Further study identified these time-clustered noise hits as caused by scintillation light from radioactivity in the PMT glass. The bump around 15 µs is caused by ionized residual gas molecules, which are produced by the collisions with the accelerated photo-electrons. Such pulses are hereafter referred to as after-pulses.

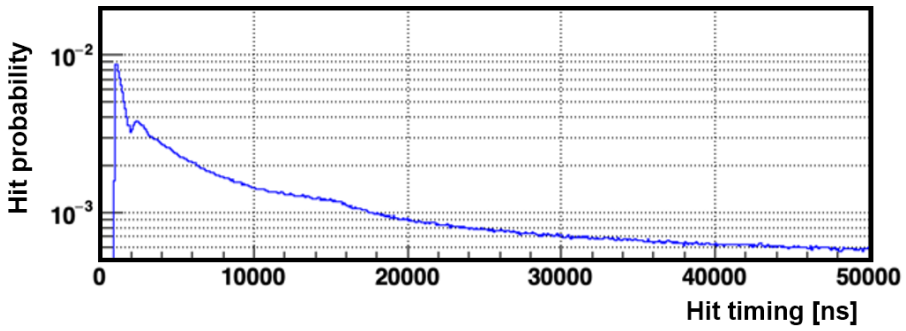

Figure 19. Timing distribution of repeated hits (noise rate) following a signal pulse above the discriminator threshold (~ 0.25 p.e.) of a 20-inch PMT. The X axis shows the timing difference of a repeated hit from the initial hit and the Y axis shows the probability of the secondary hit. The gap between 0 to 1 µs is due to the channel dead time of the readout electronics and the peak around 1.5 µs is due to the reflection of the PMT signal. The repeat noise rate decreases exponentially in time and the feature around 12 to 18 µs is due to PMT after-pulsing.

As the relative ratio of time-clustered noise to uniformly distributed random noise is different from PMT to PMT, this noise is not easy to simulate. Therefore, we use randomly triggered data to account for this time-clustered noise in the neutron tagging analysis.

B Low energy event reconstruction algorithms

We used two reconstruction algorithms to estimate the location of the neutron capture. The first is a standard low energy reconstruction tool, BONSAI, which has been used for the solar neutrino analyses in SK [26]. The BONSAI reconstruction uses timing information from PMT hits in a 1.3 µs time window.

2022 JINST 17 P10029

It performs an iterative search from a starting position, with multiple search branches fanning out from that starting position. Branches are stopped and pruned when the goodness of fit drops below a certain level. In this application, the reconstructed primary event vertex is used as the starting point for BONSAI.

The second reconstruction tool is called Neut-Fit, which was developed specifically for this analysis. Neut-Fit is a simple vertex fitter and uses the timing information from the hits within a 10 ns time window. A shrinking grid search method is used to minimize t_{rms}, defined as

$$t_{\mathrm{rms}}(\vec{x}) = \sqrt{\frac{\sum_i^{N_{10}} (t_i - t_{\mathrm{mean}})^2}{N_{10}}}, \tag{B.1}$$

where $t_{\mathrm{mean}} = \sum_i^{N_{10}} t_i / N_{10}$, and t_i is the hit timing after ToF subtraction to the vertex $\vec{x}$, respectively. As the search progresses, the search grid shrinks until the space between points on the grid becomes 0.5 cm. The algorithm is applied twice, first with a constraint that the reconstructed vertex must be within 200 cm of the primary event vertex. Hits are then ToF-corrected to this constrained neutron vertex, and these residual times are used for the calculation of neural network variables described below. For example, the number of hits within 10 ns after the Neut-Fit ToF correction (N_{10n}) is used instead of N_{10}. For the second time, Neut-Fit is applied with no constraint other than requiring the vertex being in the SK tank. This second unconstrained vertex is used for variables in the neural network which compare this vertex to the BONSAI vertex and the neutrino interaction vertex from APFit (section 4.2.13).

C Distributions of the neural network input variables for neutron tagging

In this section, distributions of all the input variables to the neural net for neutron tagging are shown from figure 20 to figure 28. In each figure, both data and the Monte-Carlo simulation outputs are shown. In each plot, the green histogram corresponds to the neutron capture signal, the blue hatched area corresponds to the background, the red histogram shows their sum and the overlaid black points show the data, respectively. Also, the red histogram is normalized to the number of neutron capture events in the atmospheric neutrino event samples from the full SK-IV data set, which spanned 3,244.39 days between October 2008 and May 2018.

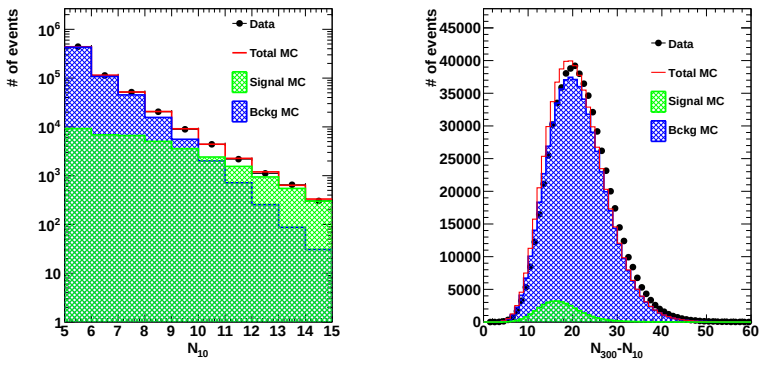

Figure 20. Distributions of the number of hits in 10 ns variable, N_{10} for $N_{10} \geq 5$ (left) and the number of hits in 300 ns variable, $N_{300} - N_{10}$ (right). The signal events tend to give larger N_{10} compared to the background. N_{10} is expected to have a larger fraction of N_{300} for the signal compared to the background.

2022 JINST 17 P10029

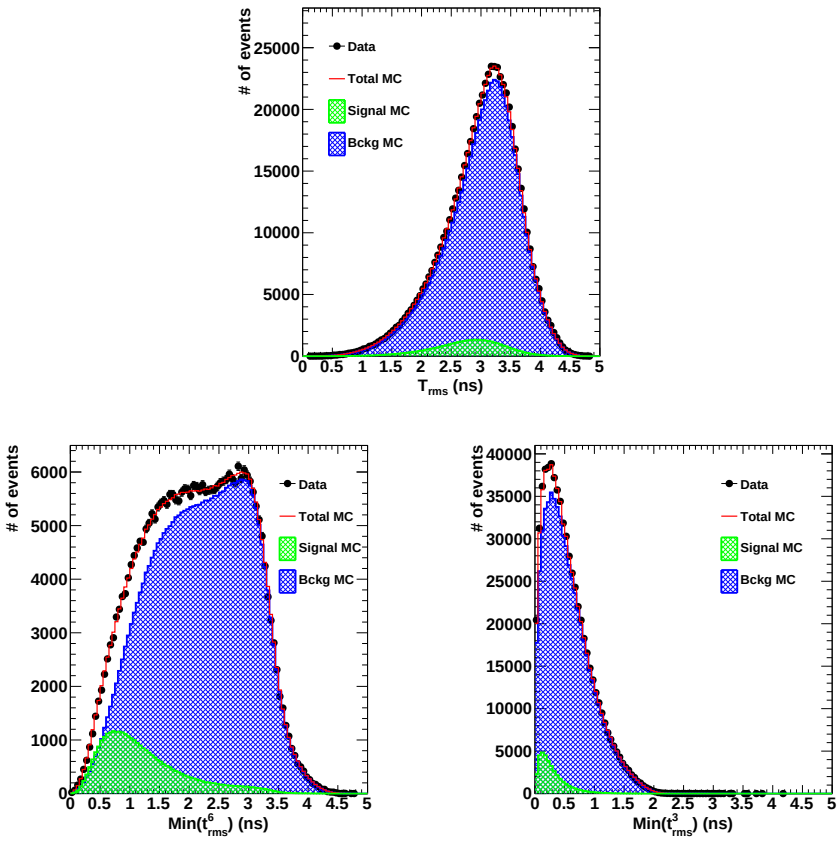

Figure 21. Distributions of the root-mean-square of the ToF-subtracted timing of candidate hits, t_{rms} (top), the minimum root-mean-square of hit timing ($\min(t_{\mathrm{rms}})$) of clusters of 6 hits, $\min(t^6_{\mathrm{rms}})$ (bottom left), and 3 hits, $\min(t^3_{\mathrm{rms}})$ (bottom right). The hits from the signal are expected to be concentrated in time and thus t_{rms}, $\min(t^6_{\mathrm{rms}})$, and $\min(t^3_{\mathrm{rms}})$ are smaller compared to the background.

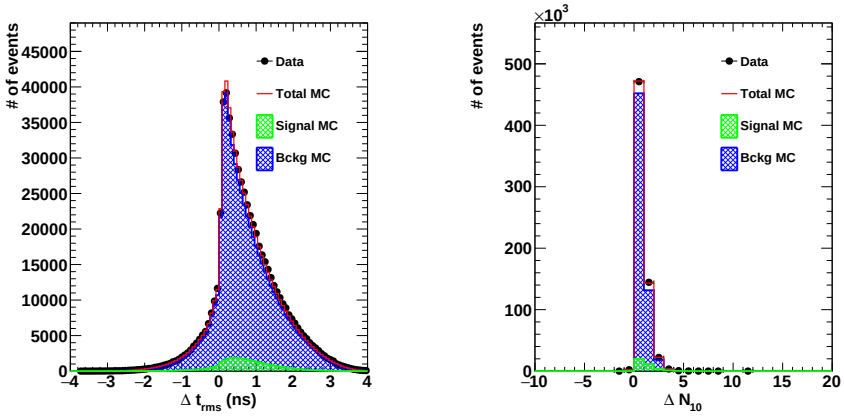

Figure 22. Distribution of the Neut-Fit root-mean-square of hit timing difference variable, Δt_{rms} (left), and the Neut-Fit number of hits in 10 ns difference variable, ΔN_{10} (right). These two variables are expected to be close to 0 for the signal because the vertexes between the two reconstructions are expected to be close for signal but not necessarily same for the background.

2022 JINST 17 P10029

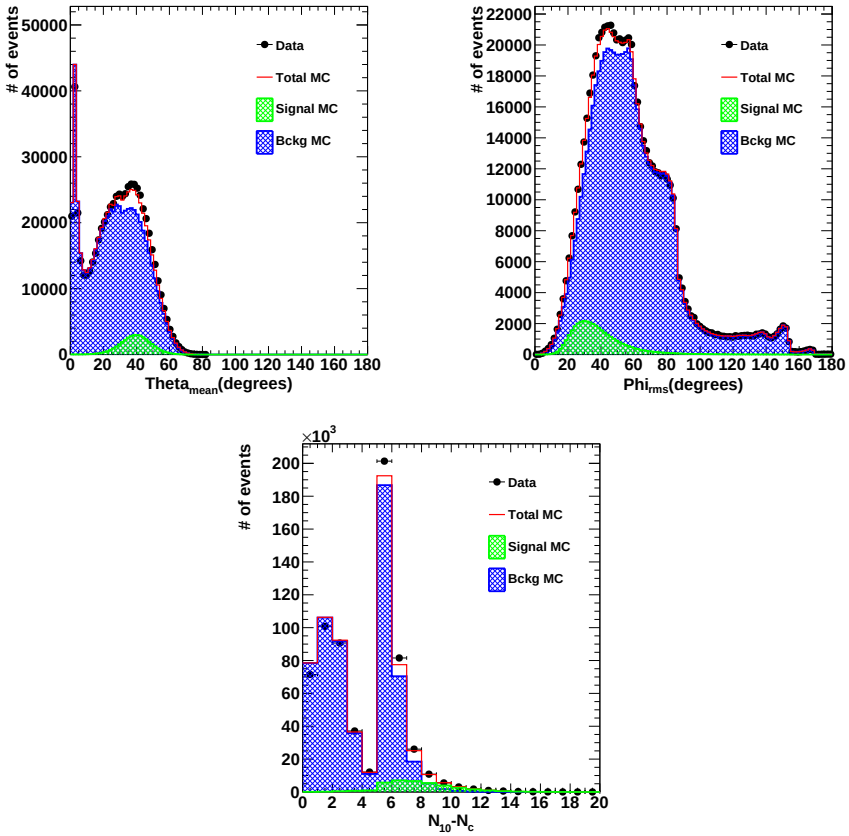

Figure 23. Distributions of mean opening angle, θ_{mean} (top left), the hit vector root-mean-square of the azimuthal angle, ϕ_{rms} (top right), and the clusters of hits variable, $N_{10} - N_{\text{c}}$ (bottom). θ_{mean} has a clear peak around 42 degrees for signal as expected. ϕ_{rms} is expected to be small for signal than background. $N_{10} - N_{\text{c}}$

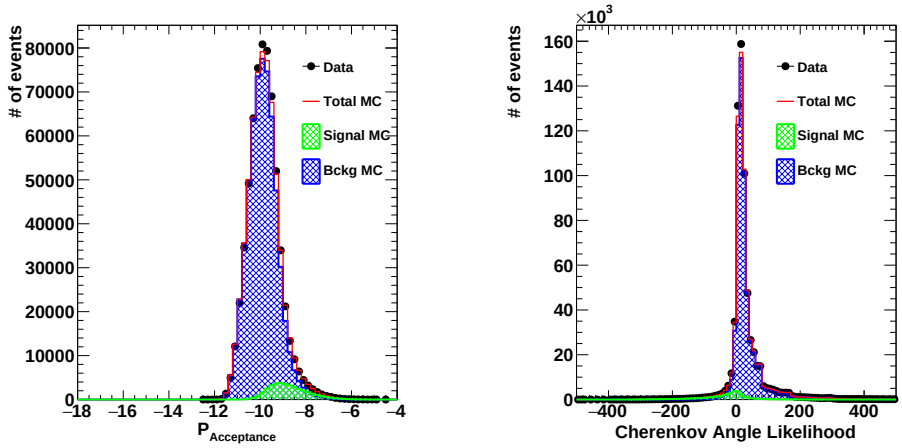

Figure 24. Distributions of the acceptance parameter, $P_{\text{Acceptance}}$ (left) and the Cherenkov angle likelihood parameter, $L_{\text{Cherenkov}}$ (right). $P_{\text{Acceptance}}$ is larger for the signal events and $L_{\text{Cherenkov}}$ is expected to be smaller for the signal, respectively.

2022 JINST 17 P10029

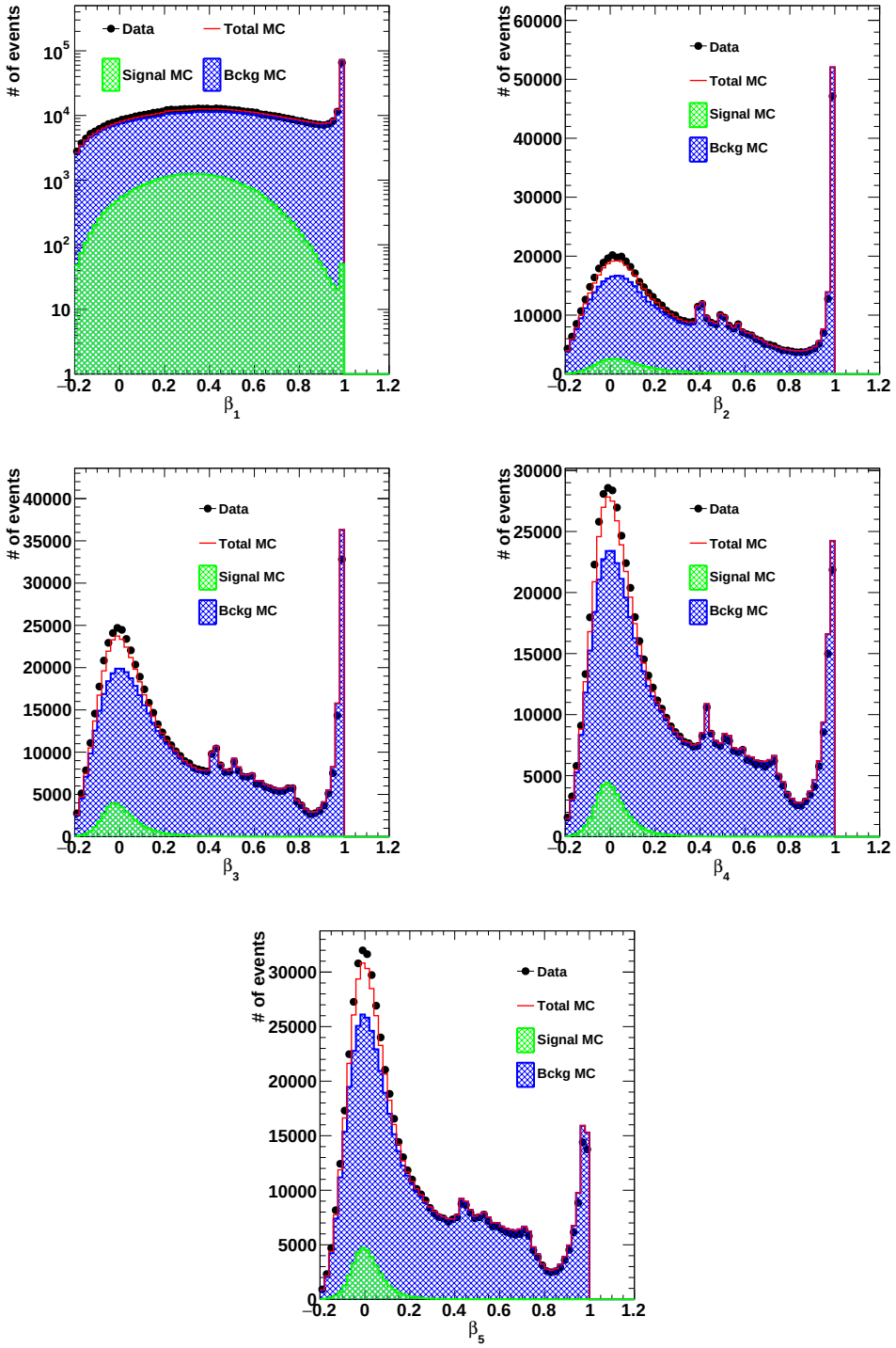

Figure 25. Isotropy parameters β_l. The signal events concentrate around 0.35 for β_1 and around 0 for other values of l, while backgrounds have broader distributions and have peaks at around 1.

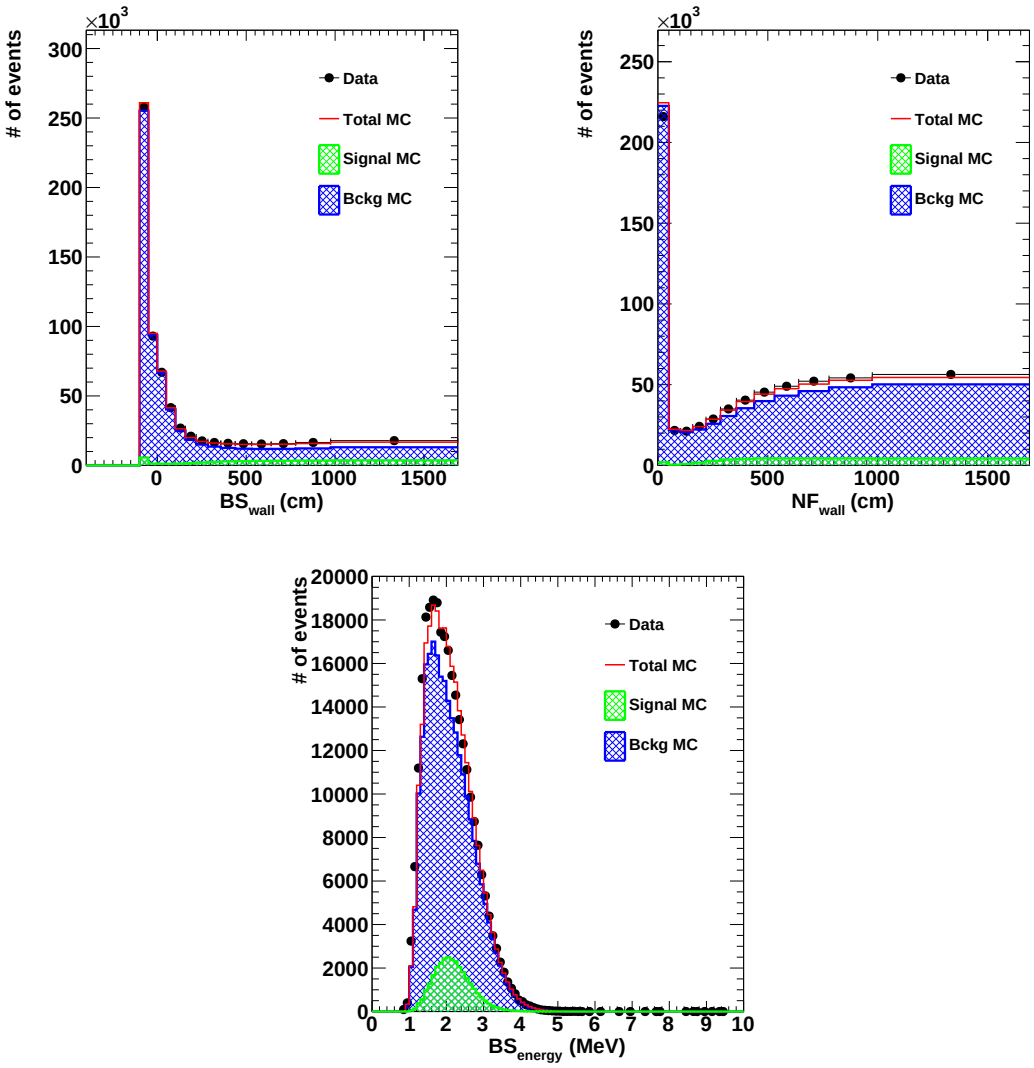

Figure 26. Distributions of the distance between the neutron vertex reconstructed by BONSAI and the nearest inner detector wall, BS_{wall} (top left), the distance between the neutron vertex reconstructed by Neut-Fit and the nearest inner detector wall, NF_{wall} (top left), and the energy reconstructed by BONSAI, BS_{energy} (bottom). The normalization of BS_{energy} is different for the signal and the background, as many background events fail to be reconstructed at this stage. The background events concentrate close to the wall but the signal does not, as shown in both top plots, BS_{wall} and NF_{wall}, if signal events are correctly reconstructed. The reconstructed energy, BS_{energy}, is expected to have peak at 2.2 MeV for signal but not for background.

2022 JINST 17 P10029

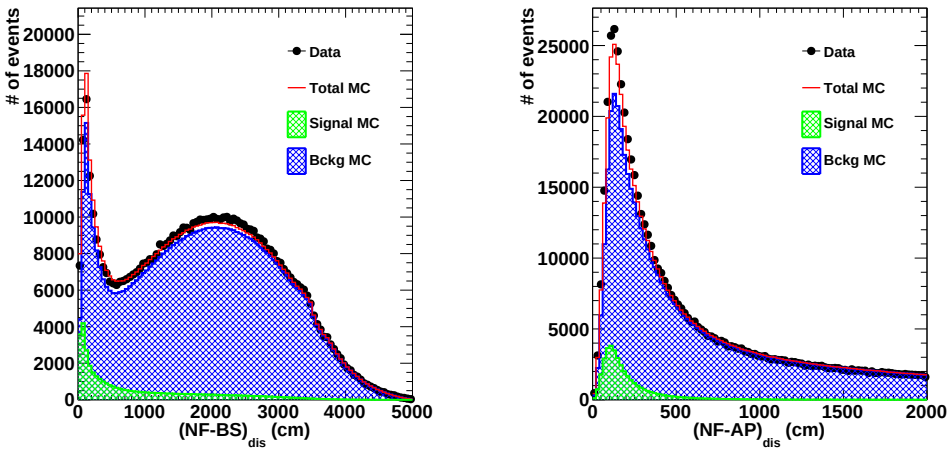

Figure 27. Distributions of the distance between the reconstructed vertices of Neut-Fit and BONSAI, $(NF-BS)_{\mathrm{dis}}$ (left), and the distance between Neut-Fit the reconstructed vertices of Neut-Fit and APFit, $(NF-AP)_{\mathrm{dis}}$, (right). These two values are expected to have a peak close to 0 because the vertexes from the two different reconstructions are expected to be similar for signal but this is not necessarily true for the background.

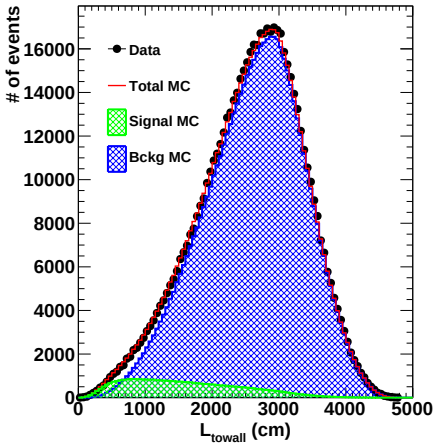

Figure 28. Distribution of the distance from Neut-Fit's reconstructed vertex to the ID wall in the direction of the particle, L_{towall}. The background events tend to have larger value compared to the signal.

D Previous analysis method

In previous analyses [10–12, 28] an older tagging algorithm was employed that did not make use of the time-clustered noise rejection and used N_{10}^{RAW} instead of N_{10} in its selections. The initial selection criteria required N_{10} to be larger than 6. In addition, the following parameters were not used in the neural network: Acceptance, Cherenkov angle, isotropy and L_{towall}. Instead, the number of hits on low-probability PMTs (N_{low}, defined below) was used. The neutron tagging efficiency was estimated to be 20.7%. With this algorithm, the neutron tagging efficiencies between Am-Be data and the MC differed by at most 20%. This value was used as the systematic uncertainty for the algorithm.

2022 JINST 17 P10029

D.1 Number of hits on low-probability PMTs: N_{low}

Noise hits are expected to be distributed in a geometrically uniform manner while real photons from γ induce a PMT position dependence because of their directionality. The PMT hit probability is defined in equation (4.4). In order to define a low-probability PMT, a threshold is defined which depends on the vertex location in the detector, as shown in figure 29.

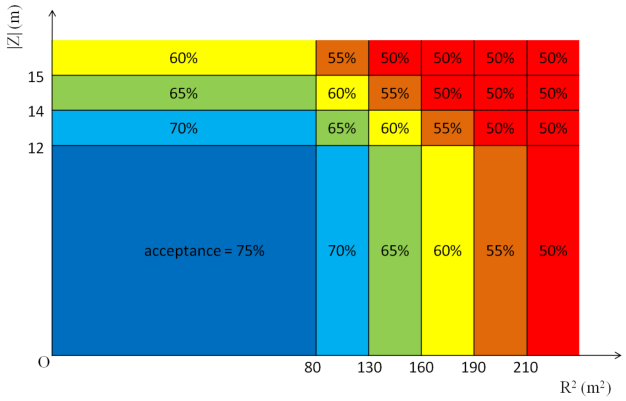

Figure 29. Varying acceptance requirements for the N_{low} cut as a function of tank coordinates.

First, PMTs are sorted in order of their photon detection probability. The probability value of each PMT is summed starting from the highest value and the running sum is compared with a threshold. When the sum exceeds this threshold the last PMT added and any remaining PMTs are regarded as low-probability PMTs. The threshold table has a vertex position dependence.

Figure 30 shows distributions of $N_{10} - N_{\mathrm{low}}$ which was used in as an input to the neural network.

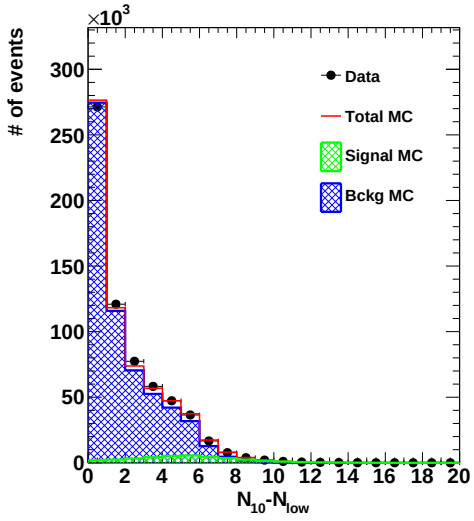

Figure 30. Hits on low-probability PMTs, $N_{10} - N_{\mathrm{low}}$. The N_{low} parameter is expected to be small for signal events. The green histogram corresponds to the neutron capture signal and the hatched area shows the background. The red histogram shows the sum of the signal and the background, which has been normalized to the number of capture events in the data (black dots).

2022 JINST 17 P10029

E Glossary

Table 6. Acronyms

General	
HV	high voltage
MC	Monte-Carlo
MLP	mulit layer perception
PMT	photo multiplier tube
ToF	time of flight
Super-Kamiokande detector	
SK	Super-Kamiokande
ID	inner detector
OD	outer detector
Event categories of SK	
FC	fully-contained
PC	partially-contained
UPMU	upward-going muon
Names of the event triggers	
SLE	super low enegry (trigger)
LE	Low energy (trigger)
HE	High energy (trigger)
SHE	super high energy (trigger)
AFT	after (trigger)
Calibration sources	
Am-Be	americium-beryllium
BGO	bismuth germanium oxide (inorganic scintillator)
Event reconstruction tools	
APFit(AP)	An event reconstruction software library developed for the atmospheric neutrino and the proton decay analyses of SK
BONSAI(BS)	An event reconstruction software library developed for the solar and supernova neutrino analyses
Neut-Fit(NF)	Newly developed simple vertex reconstruction software
Software libraries	
NEUT	A neutrino-nucleus interaction simulation program library
GEANT3	Software library of detector description and simulation
GEANT4	Software library of detector description and simulation
FLUKA	Fully integrated particle physics Monte-Carlo simulation package
GFLUKA	A version of FLUKA designed to be used with GEANT3
CALOR	Hadronic interaction simulation package
MICAP	Low energy neutron, ion and gamma ray transport software library
SKDETSIM	A detector simulation software library developed for SK
ROOT	A data analysis framework
TMLP	TMulitLayerPerception (TMLP) library

2022 JINST 17 P10029

Acknowledgments

We gratefully acknowledge the cooperation of the Kamioka Mining and Smelting Company. The Super-Kamiokande experiment has been built and operated from funding by the Japanese Ministry of Education, Culture, Sports, Science and Technology, the U.S. Department of Energy, and the U.S. National Science Foundation. Some of us have been supported by funds from the National Research Foundation of Korea NRF-2009-0083526 (KNRC) funded by the Ministry of Science, ICT, and Future Planning and the Ministry of Education (2018R1D1A3B07050696, 2018R1D1A1B07049158), the Japan Society for the Promotion of Science, the National Natural Science Foundation of China under Grants No. 11235006, the Spanish Ministry of Science, Universities and Innovation (grant PGC2018-099388-B-I00), the Natural Sciences and Engineering Research Council (NSERC) of Canada, the Scinet and Westgrid consortia of Compute Canada, the National Science Centre, Poland (2015/18/E/ST2/00758), the Science and Technology Facilities Council (STFC) and GridPP, U.K., the European Union's Horizon 2020 Research and Innovation Programme under the Marie Sklodowska-Curie grant agreement no.754496, H2020-MSCA-RISE-2018 JENNIFER2 grant agreement no.822070, and H2020-MSCA-RISE-2019 SK2HK grant agreement no. 872549.

References

[1] Super-Kamiokande collaboration, *Solar Neutrino Measurements in Super-Kamiokande-IV*, *Phys. Rev. D* **94** (2016) 052010 [arXiv:1606.07538].

[2] Super-Kamiokande collaboration, *Atmospheric neutrino oscillation analysis with external constraints in Super-Kamiokande I-IV*, *Phys. Rev. D* **97** (2018) 072001 [arXiv:1710.09126].

[3] T2K collaboration, *Evidence of Electron Neutrino Appearance in a Muon Neutrino Beam*, *Phys. Rev. D* **88** (2013) 032002 [arXiv:1304.0841].

[4] Super-Kamiokande collaboration, *Search for Nucleon Decay into Charged Anti-lepton plus Meson in Super-Kamiokande I and II*, *Phys. Rev. D* **85** (2012) 112001 [arXiv:1203.4030].

[5] Super-Kamiokande collaboration, *Supernova Relic Neutrino Search at Super-Kamiokande*, *Phys. Rev. D* **85** (2012) 052007 [arXiv:1111.5031].

[6] J.F. Beacom and M.R. Vagins, *GADZOOKS! Anti-neutrino spectroscopy with large water Cherenkov detectors*, *Phys. Rev. Lett.* **93** (2004) 171101 [hep-ph/0309300].

[7] Super-Kamiokande collaboration, *Search for proton decay via $p \to e^+\pi^0$ and $p \to \mu^+\pi^0$ with an enlarged fiducial volume in Super-Kamiokande I-IV*, *Phys. Rev. D* **102** (2020) 112011 [arXiv:2010.16098].

[8] D. Cokinos and E. Melkonian, *Measurement of the 2200 m/sec neutron-proton capture cross section*, *Phys. Rev. C* **15** (1977) 1636.

[9] Super-Kamiokande collaboration, *First Study of Neutron Tagging with a Water Cherenkov Detector*, *Astropart. Phys.* **31** (2009) 320 [arXiv:0811.0735].

[10] Super-Kamiokande collaboration, *Search for proton decay via $p \to e^+\pi^0$ and $p \to \mu^+\pi^0$ in 0.31 megaton·years exposure of the Super-Kamiokande water Cherenkov detector*, *Phys. Rev. D* **95** (2017) 012004 [arXiv:1610.03597].

2022 JINST 17 P10029

[11] Super-Kamiokande collaboration, *Search for nucleon decay into charged antilepton plus meson in 0.316 megaton·years exposure of the Super-Kamiokande water Cherenkov detector*, *Phys. Rev. D* **96** (2017) 012003 [arXiv:1705.07221].

[12] Super-Kamiokande collaboration, *Search for Boosted Dark Matter Interacting With Electrons in Super-Kamiokande*, *Phys. Rev. Lett.* **120** (2018) 221301 [arXiv:1711.05278].

[13] K. Abe et al., *Calibration of the Super-Kamiokande Detector*, *Nucl. Instrum. Meth. A* **737** (2014) 253 [arXiv:1307.0162].

[14] S. Yamada et al., *Commissioning of the new electronics and online system for the Super-Kamiokande experiment*, *IEEE Trans. Nucl. Sci.* **57** (2010) 428.

[15] M. Honda, T. Kajita, K. Kasahara and S. Midorikawa, *Improvement of low energy atmospheric neutrino flux calculation using the JAM nuclear interaction model*, *Phys. Rev. D* **83** (2011) 123001 [arXiv:1102.2688].

[16] Y. Hayato, *NEUT*, *Nucl. Phys. B Proc. Suppl.* **112** (2002) 171.

[17] R. Brun, F. Bruyant, M. Maire, A. McPherson and P. Zanarini, *Geant3: user's guide Geant 3.10, Geant 3.11*, CERN-DD-EE-84-1 (1987).

[18] Super-Kamiokande collaboration, *A Measurement of atmospheric neutrino oscillation parameters by Super-Kamiokande I*, *Phys. Rev. D* **71** (2005) 112005 [hep-ex/0501064].

[19] C. Zeitnitz and T.A. Gabriel, *The GEANT - CALOR interface and benchmark calculations of ZEUS test calorimeters*, *Nucl. Instrum. Meth. A* **349** (1994) 106.

[20] *HETC: Monte Carlo High-Energy Nucleon-Meson Transport Code*, RSIC Computer Code Collection, CCC-178, Oak Ridge National Laboratory (1977).

[21] A. Fasso et al., *FLUKA 92*, in *Proceedings of the Workshop on Simulating Accelerator Radiation Environments*, Santa Fe, NM, U.S.A., 11-115 January 1993, pp. 134–144 [Tech. Rep., LA-12835-C, Los Alamos, NM, U.S.A.].

[22] J. Johnson and T. Gabriel, *A User's Guide to MICAP: A Monte Carlo Ionization Chamber Analysis Package*, Oak Ridge National Laboratory (1988).

[23] Y. Nakano, H. Sekiya, S. Tasaka, Y. Takeuchi, R.A. Wendell, M. Matsubara et al., *Measurement of Radon Concentration in Super-Kamiokande's Buffer Gas*, *Nucl. Instrum. Meth. A* **867** (2017) 108 [arXiv:1704.06886].

[24] Y. Nakano, T. Hokama, M. Matsubara, M. Miwa, M. Nakahata, T. Nakamura et al., *Measurement of the radon concentration in purified water in the Super-Kamiokande IV detector*, *Nucl. Instrum. Meth. A* **977** (2020) 164297 [arXiv:1910.03823].

[25] R. Brun and F. Rademakers, *ROOT: An object oriented data analysis framework*, *Nucl. Instrum. Meth. A* **389** (1997) 81.

[26] M. Smy, *Low Energy Event Reconstruction and Selection in Super-Kamiokande-III*, in *Proceedings of the 30th International Cosmic Ray Conference*, Merida, Yucatan, Mexico, 3–11 July 2007, vol. 5, pp. 1279–1282.

[27] J.E. Renner, *High Pressure Xenon Detectors for Rare Physics Searches*, Ph.D. thesis, UC Berkeley, 2014.

[28] Super-Kamiokande collaboration, *Search for proton decay into three charged leptons in 0.37 megaton-years exposure of the Super-Kamiokande*, *Phys. Rev. D* **101** (2020) 052011 [arXiv:2001.08011].

2022 JINST 17 P10029

The Super-Kamiokande collaboration

K. Abe[1,46] Y. Haga[1] Y. Hayato[1,46,*] K. Hiraide[1,46] K. Ieki[1] M. Ikeda[1] S. Imaizumi[1] K. Iyogi[1] J. Kameda[1,46] Y. Kanemura[1] Y. Kataoka[1,46] Y. Kato[1] Y. Kishimoto[1,46,a] S. Miki[1] S. Mine[1] M. Miura[1,46] T. Mochizuki[1] S. Moriyama[1,46] Y. Nagao[1] M. Nakahata[1,46] T. Nakajima[1] Y. Nakano[1] S. Nakayama[1,46] T. Okada[1] K. Okamoto[1] A. Orii[1,b] K. Sato[1] H. Sekiya[1] M. Shiozawa[1,46] Y. Sonoda[1] Y. Suzuki[1] A. Takeda[1,46] Y. Takemoto[1,46] A. Takenaka[1,c] H. Tanaka[1,46] S. Tasaka[1] T. Tomura[1,46,d] K. Ueno[1,e] S. Watanabe[1] T. Yano[1] T. Yokozawa[1,d] S. Han[2] T. Irvine[2] T. Kajita[2,22,46] I. Kametani[2] K. Kaneyuki[2,46,†] K.P. Lee[2] T. McLachlan[2] K. Okumura[2,46] E. Richard[2] T. Tashiro[2] R. Wang[2] J. Xia[2] G.D. Megias[3] D. Bravo-Berguño[4] L. Labarga[4] B. Zaldivar[4] M. Goldhaber[5,†] F. d. M. Blaszczyk[6,f] J. Gustafson[6] C. Kachulis[6] E. Kearns[6,46] J.L. Raaf[6,f] J.L. Stone[6,46] L.R. Sulak[6] S. Sussman[6] L. Wan[6] T. Wester[6] B.W. Pointon[7,52] J. Bian[8] G. Carminati[8] M. Elnimr[8] N.J. Griskevich[8] W.R. Kropp[8,†] S. Locke[8] A. Renshaw[8,g] M.B. Smy[8] H.W. Sobel[8,46] V. Takhistov[8,46] P. Weatherly[8] K.S. Ganezer[9,†] B.L. Hartfiel[9] J. Hill[9] W.E. Keig[9] N. Hong[10] J.Y. Kim[10] I.T. Lim[10] R.G. Park[10] T. Akiri[11] B. Bodur[11] A. Himmel[11,f] Z. Li[11,h] E. O'Sullivan[11,i] K. Scholberg[11,46] C.W. Walter[11,46] T. Wongjirad[11,j] L. Bernard[12] A. Coffani[12] O. Drapier[12] S. El Hedri[12] A. Giampaolo[12] J. Imber[12] Th.A. Mueller[12] P. Paganini[12] B. Quilain[12] T. Ishizuka[13] T. Nakamura[14] J.S. Jang[15] K. Choi[16,k] J.G. Learned[16] S. Matsuno[16] S.N. Smith[16] J. Amey[17] L.H.V. Anthony[17] R.P. Litchfield[17,l] W.Y. Ma[17,m] D. Marin[17] A.A. Sztuc[17] Y. Uchida[17] M.O. Wascko[17] V. Berardi[18] M.G. Catanesi[18] R.A. Intonti[18] E. Radicioni[18] N.F. Calabria[19] G. De Rosa[19] L.N. Machado[19] G. Collazuol[20] F. Iacob[20] M. Lamoureux[20] N. Ospina[20] L. Ludovici[21] M. Gonin[22] G. Pronost[22] Y. Maekawa[23] Y. Nishimura[23] S. Cao[24,n] M. Friend[24] T. Hasegawa[24] T. Ishida[24] T. Ishii[24] M. Jakkapu[24] T. Kobayashi[24] T. Matsubara[24] T. Nakadaira[24] K. Nakamura[24,46] Y. Oyama[24] K. Sakashita[24] T. Sekiguchi[24] T. Tsukamoto[24] T. Boschi[25] F. Di Lodovico[25] J. Migenda[25] S. Molina Sedgwick[25,o] M. Taani[25] S. Zsoldos[25] K.E. Abe[26] M. Hasegawa[26] Y. Isobe[26] Y. Kotsar[26] H. Miyabe[26] H. Ozaki[26] T. Shiozawa[26] T. Sugimoto[26] A.T. Suzuki[26] Y. Takeuchi[26,46] S. Yamamoto[26] A. Ali[27,p] Y. Ashida[27,q] C. Bronner[27] J. Feng[27] T. Hayashino[27] T. Hiraki[27,r] S. Hirota[27] K. Huang[27] M. Jiang[27] T. Kikawa[27] M. Mori[27,s] A. Murakami[27] KE. Nakamura[27] T. Nakaya[27,46] N.D. Patel[27] K. Suzuki[27,b] S. Takahashi[27,b] K. Tateishi[27] R.A. Wendell[27,46] K. Yasutome[27] P. Fernandez[28,t] N. McCauley[28] P. Mehta[28] A. Pritchard[28] K.M. Tsui[28] Y. Fukuda[29] Y. Itow[30,31] H. Menjo[30] G. Mitsuka[30,b] M. Murase[30] F. Muto[30] T. Niwa[30] T. Suzuki[30] M. Tsukada[30] K. Frankiewicz[32,u] P. Mijakowski[32] J. Hignight[33,v] J. Jiang[33] C.K. Jung[33] X. Li[33] J.L. Palomino[33,w] G. Santucci[33,x] C. Vilela[33,y] M.J. Wilking[33] C. Yanagisawa[33,z] D. Fukuda[34] K. Hagiwara[34] M. Harada[34] T. Horai[34] H. Ishino[34] S. Ito[34] T. Kayano[34] A. Kibayashi[34] H. Kitagawa[34] Y. Koshio[34,46] W. Ma[34] T. Mori[34] H. Nagata[34] N. Piplani[34] S. Sakai[34] M. Sakuda[34] Y. Takahira[34] C. Xu[34] R. Yamaguchi[34] Y. Kuno[35] G. Barr[36] D. Barrow[36] L. Cook[36,46] A. Goldsack[36,46] S. Samani[36] C. Simpson[36,46] D. Wark[36,42] F. Nova[37] R. Tacik[38,52] J.Y. Yang[39] A. Cole[40] S.J. Jenkins[40] M. Malek[40] J.M. McElwee[40] O. Stone[40] M.D. Thiesse[40] L.F. Thompson[40] H. Okazawa[41] Y. Choi[43] S.B. Kim[43] I. Yu[43] A.K. Ichikawa[44] K. Nakamura[44] K. Ito[45] K. Nishijima[45] R.G. Calland[46] P. de Perio[46] K. Martens[46] M. Murdoch[46] M.R. Vagins[46,8] M. Koshiba[47,†] Y. Totsuka[47,†] K. Iwamoto[48] Y. Nakajima[48,46] N. Ogawa[48] Y. Suda[48] M. Yokoyama[48,46] D. Hamabe[49] S. Izumiyama[49] M. Kuze[49] Y. Okajima[49] M. Tanaka[49] T. Yoshida[49] M. Inomoto[50] M. Ishitsuka[50] H. Ito[50] R. Matsumoto[50] K. Ohta[50] M. Shinoki[50] J.F. Martin[51] C.M. Nantais[51] H.A. Tanaka[51] T. Towstego[51] R. Akutsu[52] M. Hartz[52] A. Konaka[52] N.W. Prouse[52] S. Chen[53] B.D. Xu[53] Y. Zhang[53] S. Berkman[54,f] S. Tobayama[54] K. Connolly[55] R.J. Wilkes[55] M. Posiadala-Zezula[56] D. Hadley[57] B. Richards[57] B. Jamieson[58] J. Walker[58] Ll. Marti[59] A. Minamino[59] K. Okamoto[59] G. Pintaudi[59] S. Sano[59] R. Sasaki[59]

[1] *Kamioka Observatory, Institute for Cosmic Ray Research, University of Tokyo, Kamioka, Gifu 506-1205, Japan*

[2] *Research Center for Cosmic Neutrinos, Institute for Cosmic Ray Research, University of Tokyo, Kashiwa, Chiba 277-8582, Japan*

[3] *Institute for Cosmic Ray Research, University of Tokyo, Kashiwa, Chiba 277-8582, Japan*

2022 JINST 17 P10029

[4] *Department of Theoretical Physics, University Autonoma Madrid, 28049 Madrid, Spain*
[5] *Physics Department, Brookhaven National Laboratory, Upton, NY 11973, U.S.A.*
[6] *Department of Physics, Boston University, Boston, MA 02215, U.S.A.*
[7] *Department of Physics, British Columbia Institute of Technology, Burnaby, BC, V5G 3H2, Canada*
[8] *Department of Physics and Astronomy, University of California, Irvine, Irvine, CA 92697-4575, U.S.A.*
[9] *Department of Physics, California State University, Dominguez Hills, Carson, CA 90747, U.S.A.*
[10] *Institute for Universe and Elementary Particles, Chonnam National University, Gwangju 61186, Korea*
[11] *Department of Physics, Duke University, Durham NC 27708, U.S.A.*
[12] *Ecole Polytechnique, IN2P3-CNRS, Laboratoire Leprince-Ringuet, F-91120 Palaiseau, France*
[13] *Junior College, Fukuoka Institute of Technology, Fukuoka, Fukuoka 811-0295, Japan*
[14] *Department of Physics, Gifu University, Gifu, Gifu 501-1193, Japan*
[15] *GIST College, Gwangju Institute of Science and Technology, Gwangju 500-712, Korea*
[16] *Department of Physics and Astronomy, University of Hawaii, Honolulu, HI 96822, U.S.A.*
[17] *Department of Physics, Imperial College London , London, SW7 2AZ, United Kingdom*
[18] *Dipartimento Interuniversitario di Fisica, INFN Sezione di Bari and Università e Politecnico di Bari, I-70125, Bari, Italy*
[19] *Dipartimento di Fisica, INFN Sezione di Napoli and Università di Napoli, I-80126, Napoli, Italy*
[20] *Dipartimento di Fisica, INFN Sezione di Padova and Università di Padova, I-35131, Padova, Italy*
[21] *INFN Sezione di Roma and Università di Roma "La Sapienza", I-00185, Roma, Italy*
[22] *ILANCE, CNRS — University of Tokyo International Research Laboratory, Kashiwa, Chiba 277-8582, Japan*
[23] *Department of Physics, Keio University, Yokohama, Kanagawa, 223-8522, Japan*
[24] *High Energy Accelerator Research Organization (KEK), Tsukuba, Ibaraki 305-0801, Japan*
[25] *Department of Physics, King's College London, London, WC2R 2LS, U.K.*
[26] *Department of Physics, Kobe University, Kobe, Hyogo 657-8501, Japan*
[27] *Department of Physics, Kyoto University, Kyoto, Kyoto 606-8502, Japan*
[28] *Department of Physics, University of Liverpool, Liverpool, L69 7ZE, United Kingdom*
[29] *Department of Physics, Miyagi University of Education, Sendai, Miyagi 980-0845, Japan*
[30] *Institute for Space-Earth Environmental Research, Nagoya University, Nagoya, Aichi 464-8602, Japan*
[31] *Kobayashi-Maskawa Institute for the Origin of Particles and the Universe, Nagoya University, Nagoya, Aichi 464-8602, Japan*
[32] *National Centre For Nuclear Research, 02-093 Warsaw, Poland*
[33] *Department of Physics and Astronomy, State University of New York at Stony Brook, NY 11794-3800, U.S.A.*
[34] *Department of Physics, Okayama University, Okayama, Okayama 700-8530, Japan*
[35] *Department of Physics, Osaka University, Toyonaka, Osaka 560-0043, Japan*
[36] *Department of Physics, Oxford University, Oxford, OX1 3PU, United Kingdom*
[37] *Rutherford Appleton Laboratory, Harwell, Oxford, OX11 0QX, U.K.*
[38] *Department of Physics, University of Regina, 3737 Wascana Parkway, Regina, SK, S4SOA2, Canada*
[39] *Department of Physics, Seoul National University, Seoul 151-742, Korea*
[40] *Department of Physics and Astronomy, University of Sheffield, S3 7RH, Sheffield, United Kingdom*
[41] *Department of Informatics in Social Welfare, Shizuoka University of Welfare, Yaizu, Shizuoka, 425-8611, Japan*
[42] *STFC, Rutherford Appleton Laboratory, Harwell Oxford, and Daresbury Laboratory, Warrington, OX11 0QX, United Kingdom*
[43] *Department of Physics, Sungkyunkwan University, Suwon 440-746, Korea*
[44] *Department of Physics, Faculty of Science, Tohoku University, Sendai, Miyagi 980-8578, Japan*
[45] *Department of Physics, Tokai University, Hiratsuka, Kanagawa 259-1292, Japan*
[46] *Kavli Institute for the Physics and Mathematics of the Universe (WPI), The University of Tokyo Institutes for Advanced Study, University of Tokyo, Kashiwa, Chiba 277-8583, Japan*
[47] *The University of Tokyo, Bunkyo, Tokyo 113-0033, Japan*
[48] *Department of Physics, University of Tokyo, Bunkyo, Tokyo 113-0033, Japan*
[49] *Department of Physics,Tokyo Institute of Technology, Meguro, Tokyo 152-8551, Japan*
[50] *Department of Physics, Faculty of Science and Technology, Tokyo University of Science, Noda, Chiba 278-8510, Japan*

2022 JINST 17 P10029

[51] *Department of Physics, University of Toronto, ON, M5S 1A7, Canada*
[52] *TRIUMF, 4004 Wesbrook Mall, Vancouver, BC, V6T2A3, Canada*
[53] *Department of Engineering Physics, Tsinghua University, Beijing, 100084, China*
[54] *Department of Physics and Astronomy, University of British Columbia, Vancouver, BC, V6T1Z4, Canada*
[55] *Department of Physics, University of Washington, Seattle, WA 98195-1560, U.S.A.*
[56] *Faculty of Physics, University of Warsaw, Warsaw, 02-093, Poland*
[57] *Department of Physics, University of Warwick, Coventry, CV4 7AL, U.K.*
[58] *Department of Physics, University of Winnipeg, MB R3J 3L8, Canada*
[59] *Faculty of Engineering, Yokohama National University, Yokohama, Kanagawa, 240-8501, Japan*

[*] *Corresponding author.*
[a] *Currently at Research Center for Neutrino Science, Tohoku University, Sendai 980-8578, Japan.*
[b] *Currently at High Energy Accelerator Research Organization (KEK), Tsukuba, Ibaraki 305-0801, Japan.*
[c] *Currently at School of Physics and Astronomy, Shanghai Jiao Tong University, Shanghai, China.*
[d] *Currently at Institute for Cosmic Ray Research, University of Tokyo, Kashiwa, Chiba 277-8582, Japan.*
[e] *Currently at Research Center for the Early Universe (RESCEU), Graduate School of Science, The University of Tokyo, Tokyo 113-0033, Japan.*
[f] *Currently at Fermi National Accelerator Laboratory, Batavia, IL 60510, U.S.A.*
[g] *Currently at Department of Physics, University of Houston, Houston, TX 77204, U.S.A.*
[h] *Currently at Institute of High Energy Physics, Chinese Academy of Sciences, Beijing, 100049 China.*
[i] *Currently at Department of Physics and Astronomy, Uppsala University, Box 516, S-75120 Uppsala, Sweden.*
[j] *Currently at Department of physics and astronomy, Tufts University, Medford, MA, 02155, U.S.A.*
[k] *Currently at Institute for Basic Science (IBS), Dajeon, 34126, Korea.*
[l] *Currently at School of Physics and Astronomy, University of Glasgow, Glasgow, G12 8QQ, United Kingdom.*
[m] *Currently at DESY, D-15738 Zeuthen, Germany.*
[n] *Currently at Institute for Interdisciplinary Research in Science and Education, ICISE, Quy Nhon, 55121, Vietnam.*
[o] *Currently at Department de Fisica Teorica, Universitat de Valencia, and Instituto de Fisica Corpuscular, CSIC, Universitat de Valencia, 46980 Paterna, Spain.*
[p] *Currently at University of Winnipeg, R3B2E9, Canada.*
[q] *Currently at Department of Physics and Wisconsin IceCube Particle Astrophysics Center, University of Wisconsin-Madison, Madison, WI 53706, U.S.A.*
[r] *Currently at Research Institute for Interdisciplinary Science, Okayama University, Okayama, Okayama 700-8530, Japan.*
[s] *Currently at Department of Earth Science and Astronomy, The University of Tokyo, Tokyo 153-8902, Japan.*
[t] *Currently at Donostia International Physics Center, Donostia, 20018, Spain.*
[u] *Currently at Department of Physics, Boston University, Boston, MA 02215, U.S.A.*
[v] *Currently at Dept. of Physics, University of Alberta, Edmonton, Alberta, T6G 2E1, Canada.*
[w] *Currently at Department of Physics, Illinois Institute of Technology, Chicago, 60616, IL, U.S.A.*
[x] *Currently at Department of Physics and Astronomy, York University, Toronto, Ontario, Canada.*
[y] *Currently at EP Department, CERN, 1211 Geneva 24, Switzerland.*
[z] *Also at BMCC/CUNY, Science Department, New York New York, 1007, U.S.A.*
[†] *Deceased.*

2022 JINST 17 P10029